Estimating Ion Temperatures at the Polar Coronal Hole Boundary

Yingjie Zhu (朱英杰) [ID],[1,*] Judit Szente [ID],[1] and Enrico Landi [ID][1]

[1]*Department of Climate and Space Sciences and Engineering, University of Michigan,
Ann Arbor, MI 48109, USA*

ABSTRACT

Physical quantities, such as ion temperature and nonthermal velocity, provide critical information about the heating mechanism of the million-degree solar corona. We determined the possible ion temperature T_i intervals using extreme ultraviolet (EUV) line widths, only assuming that the plasma nonthermal velocity is the same for all ions. We measured ion temperatures at the polar coronal hole boundary simultaneously observed in 2007 by the EUV Imaging Spectrometer (EIS) on board the Hinode satellite and the Solar Ultraviolet Measurements of Emitted Radiation (SUMER) on board the Solar and Heliospheric Observatory (SOHO). The temperatures of ions with the charge-to-mass ratio (Z/A) less than 0.20 or greater than 0.33 are much higher than the local electron temperature. The measured ion temperature decreases with the Z/A to 0.25 and then increases with the charge-to-mass ratio. We ran the Alfvén Wave Solar Model-realtime (AWSoM-R) and the SPECTRUM module to validate the ion temperature diagnostic technique and to help interpret the results. We suggest that the widths of hot lines in the coronal hole (e.g., Fe XII, Fe XIII) are also affected by the solar wind bulk motions along the line of sight. We discussed the factors that might affect the line width fitting, including the instrumental width and non-Gaussian wings in some bright SUMER lines that can be fitted by a double-Gaussian or a κ distribution. Our study confirms the presence of preferential heating of heavy ions in coronal holes and provides new constraints to coronal heating models.

1. INTRODUCTION

The heating of the million-degree solar corona above the photosphere has been one of the major mysteries in solar physics research since the 1940s. The energy fluxes to heat different coronal structures range among 3×10^5 (quiet Sun), 8×10^5 (coronal holes) and $10^7 \, \mathrm{erg \, cm^{-2} \, s^{-1}}$ (active regions, Withbroe & Noyes 1977). The coronal holes are the darkest areas in the extreme ultraviolet (EUV) or X-Ray images on the solar disk and off-limb due to the low-density (Cranmer 2009). The open magnetic field structure and the associated fast solar wind make the coronal holes an excellent laboratory to study the mechanisms of coronal heating and solar wind acceleration, especially the wave dissipation and turbulence

Corresponding author: Yingjie Zhu (朱英杰)

yjzhu@umich.edu

* DKIST Ambassador

models (e.g., Hollweg & Isenberg 2002; Cranmer et al. 2007). Distinguishing the contribution of these proposed mechanisms requires measurements of physical properties such as electron temperature, ion temperature, and nonthermal motions in the polar coronal hole (e.g., Wilhelm 2012).

The thermal width of the spectral line is the only remote-sensing measurement of ion temperatures T_i in the corona (Del Zanna & Mason 2018). Observations from the Solar Ultraviolet Measurements of Emitted Radiation (SUMER, Wilhelm et al. 1995) on board the Solar and Heliospheric Observatory (SOHO, Domingo et al. 1995) found that the spectral lines in the coronal holes below $1.5 \, R_\odot$ are much broader than the profiles in streamers. The ion temperatures of Ne, Mg, Fe, and S are more than 2.5 times higher than their formation temperatures (Seely et al. 1997). In the darkest region of coronal holes, extreme effective temperatures of 10^7 and $2.3 \times 10^7 \, \mathrm{K}$ are found in Si VIII and Ne VIII profiles, respectively (Wilhelm et al. 1998; Wilhelm 1999).

Meanwhile, observations from the Ultraviolet Corona-graph Spectrometer (UVCS, Kohl et al. 1995) on board SOHO indicated that O VI and Mg X ions are preferentially heated to $10^7 - 10^8$ K compared to the protons above the polar coronal hole between 1.35 and $3\,R_\odot$, where ion collisions become infrequent (e.g., Kohl et al. 1997; Esser et al. 1999; Doyle et al. 1999). Significant O VI temperature-anisotropy perpendicular to the field lines are also found using the Doppler dimming or pumping of O VI 1032/1037 Å lines (e.g., Kohl et al. 1998; Li et al. 1998). It is also suggested that the solar wind expansion and the integration of optically thin emission along the line of sight (LOS) might affect the observed line widths above the coronal hole (e.g., Akinari 2007; Gilly & Cranmer 2020).

The ion-cyclotron resonance is one of the promising candidates for explaining the preferential and anisotropic heating of heavy ions (e.g., Marsch et al. 1982; Isenberg & Hollweg 1983). The heating might occur when heavy-ion particles interact with the waves generated through turbulent cascade (e.g., Hu & Habbal 1999), or via activity in the chromospheric network (e.g., Tu & Marsch 1997), or by the local instability (e.g., Markovskii & Hollweg 2004). Alternatively, heavy ions can be heated naturally in an equivalent second-order Fermi acceleration with parallel-propagating ion-cyclotron waves (Isenberg & Vasquez 2007, 2009). The presence of high-frequency waves at the ion gyrofrequency in the inner heliosphere suggests that the heavy ions might be heated and accelerated through wave-particle interaction (e.g., Kasper et al. 2013; Bowen et al. 2020), which is also found in various corona- and solar-wind models (e.g., Cranmer et al. 1999; Hu et al. 2000).

As the wave-particle interaction is sensitive to the gyrofrequency of various heavy ions, the ion charge-to-mass ratio (Z/A) plays an essential role in determining the heating efficiency of ion-cyclotron resonance (e.g., Patsourakos et al. 2002). However, only a few systematic studies of the dependence of T_i on Z/A have been made using remote sensing observations of the solar corona. Early studies used SOHO/SUMER and reached different conclusions. Tu et al. (1998, 1999) found that ion temperature T_i remains constant or slightly decreases with the increasing Z/A in the polar coronal hole. Dolla & Solomon (2008, 2009) also reported that the ion temperature T_i decreases with the increase in Z/A, but the low Z/A species (i.e., Fe VIII and Fe X) are significantly heated. Wilhelm et al. (2005) found a linear relationship between T_i and Z/A in the quiet Sun only if the Ca XIII and Fe XVII widths are discarded. Landi (2007) investigated the SUMER quiet Sun observations during different solar activity levels and concluded no cor-

relation between T_i and Z/A. On the other hand, a non-monotonic dependence of T_i on Z/A in the corona hole was found by Landi & Cranmer (2009).A couple of studies used observations from the EUV Imaging Spectrometer (EIS, Culhane et al. 2007) on board the Hinode (Kosugi et al. 2007) satellite to study ion temperature T_i in different regions. It was found that T_i decreases with Z/A in the off-limb polar coronal hole (Hahn et al. 2010). However, in the quiet Sun, T_i of different ions appears to be constant (Hahn & Savin 2014). Hahn & Savin (2013a) study the ion temperature anisotropy in an on-disk coronal hole and found that only the perpendicular ion temperature $T_{i,\perp}$ shows a dependence on Z/A while the parallel ion temperature $T_{i,\parallel}$ is rather constant.

One of the difficulties in measuring ion temperatures from the thermal width is that it is coupled with the nonthermal width, which is widely suggested as the evidence of low-frequency wave propagation in the coronal hole (e.g., Boland et al. 1975; Esser et al. 1987). Therefore, additional assumptions about either the thermal widths or nonthermal widths have to be made to decouple the two terms in observations, including T_i equals the line formation temperature (Hassler et al. 1990), the constant nonthermal widths for all ions (Tu et al. 1998), and more complicated assumptions based on the nature of waves (e.g., Dolla & Solomon 2008; Hahn & Savin 2013b).

In this study, we continued to study the dependence of ion temperature T_i on Z/A in the polar coronal hole. To have a better Z/A coverage and cross-reference between different instruments, we used a coordinated observation made by SOHO/SUMER and Hinode/EIS for the first time to address this problem. We used the method proposed by Tu et al. (1998) to separate the thermal and nonthermal widths to minimize the additional assumptions. Furthermore, we performed the global magnetohydrodynamic (MHD) simulation to validate the method to measure ion temperatures. We describe the data reduction and analysis and MHD simulation in Section 2. Section 3 shows the measured ion temperatures T_i versus Z/A and compares the observed and the synthetic profiles. We discussed the factors affecting our diagnostics in Section 4. Section 5 summarizes this study.

2. METHODOLOGY

2.1. Observation and Data Reduction

On 2007 November 16, SOHO/SUMER and Hinode/EIS made a coordinated observation of the off-limb coronal hole boundary region at the north pole (see Figure 1). SUMER observed this region from 09:01 UT to

10:03 UT. The center of the $4'' \times 300''$ SUMER slit one was pointed to $(230'', 1120'')$, which covers the off-limb plasma from around 1.01 to $1.32 R_\odot$. SUMER observed the solar UV spectrum in four 45 Å wide spectrum windows using detector B. The four windows covered first-order wavelengths of 672 to 717 Å, 746 to 791 Å, 1015 to 1060 Å, and 1210 to 1255 Å. SUMER made three 300 second exposures in each window. EIS observed this coronal hole from 07:26 UT to 08:01 UT in EUV ranging from 170 to 210 Å (short wavelength, SW) and 245 to 290 Å (long wavelength, LW). The corrected pointing of the EIS $2'' \times 512''$ slit two was centered around $850''$ in Solar-Y. In the x direction, EIS performed a seven-step raster scan from $232.5''$ to $246.5''$. The off-limb portion of the EIS slit covered the coronal hole plasma from about 1.00 to $1.15 R_\odot$ (depending on the wavelength due to the tilt of the EIS grating and spatial offset between two EIS CCDs). EIS and SUMER have a spatial resolution of $1''$ along the slit. We note that Hahn et al. (2010) used the same EIS data set to study the ion temperature in the polar coronal hole, but we processed the EIS data with the latest EIS calibrations that were not available back then.

We retrieved the SUMER data from the original telemetry through the SUMER Image Database. Then we applied the standard data corrections and calibrations described in the SUMER Data Cookbook, including decompression, reversion, dead-time correction, flat-field correction, local-gain correction, and geometric distortion correction. We determined the illuminated portion of the entire 1024×360 SUMER detector, which is about 300 pixels in the y direction, by manually checking the intensity distribution along the y direction in the four spectral windows. Then we resized the images in photon count rates per pixel to 1024×300 using the IDL `congrid` function. We calculated the uncertainty of the SUMER intensity in each pixel assuming that the uncertainty is dominated by the photon shot noise following Poisson statistics (Peter & Judge 1999), namely:

$$\sigma_P = \sqrt{P} \tag{1}$$

where P is the total photon counts per pixel and σ_P is the corresponding uncertainty. The uncertainty of the radiometrically calibrated intensity I is given by (Young 2019):

$$\frac{\sigma_I}{I} = \frac{\sigma_P}{P} \tag{2}$$

Since SUMER does not provide onboard wavelength calibration, we calibrated the wavelength across the detector by performing linear regression between strong coronal line centroids (in detector pixels) to the wavelengths provided by the CHIANTI atomic database (Dere et al.

1997; Del Zanna et al. 2021). The calibrated pixel sizes in Angstrom show a difference of less than 0.5% with the values given by `magnification.pro`. No absolute wavelength calibration is performed, as we only used the line width and intensity in the following diagnostics. Finally, we applied the latest (Epoch 9) SUMER radiometric calibration to the individual spectral line before the fitting.

We obtained the EIS level-0 FITS files from the Hinode Science Data Center Europe Archive. We first calibrated the EIS data set to level 1 using the IDL routine `eis_prep` (Young 2019). The level 1 data set contains the intensity after the original laboratory radiometric calibration. The uncertainty in level 1 data consists of the photon shot noise and the CCD readout noise. Then we applied the additional corrections to the level-1 data set, including the Y-offset of the CCD (Young 2011a) and the tilt of the slit (Young 2010). Since ion temperature diagnostics only relies on the widths of the spectral lines, additional radiometric corrections (i.e., Del Zanna 2013; Warren et al. 2014) were only implemented on the intensity of the spectral lines used for electron density and temperature diagnostics (see Section 2.4 for details) after data fitting. We averaged all seven EIS rasters to increase the signal-to-noise ratio (S/N).

We checked the global solar corona images taken by the Extreme-Ultraviolet Imaging Telescope (EIT, Delaboudinière et al. 1995) on board the SOHO spacecraft for context. SUMER, EIS, and EIT were coaligned manually in the following two steps: (1) we coaligned EIT and EIS by comparing the on-disk features in the EIT 195 Å image and the EIS SW spectrum filtered by the effective area of the EIT 195 Å quadrant. (2) we empirically coaligned SUMER and EIS by comparing the slope of the intensity of O VI 184.1 Å (EIS) and 1031.9 Å (SUMER) along the slit. No coalignment in the east-west direction is performed between the EIS and SUMER data. The uncertainty of the coalignment between EIT and EIS is less than $5''$ (EIT pixel size), since the features on the disk are well matched. However, since the off-limb SUMER images do not contain any features (e.g., limb brightening), coaligned EIS and SUMER images might have a residual offset of $10''$ to $15''$ in the north-south direction.

Finally, to maximize the number of observed ions, we averaged the 30 pixels (blue line in Figure 1) between 1.01 and 1.04 solar radii by averaging the observed intensities for further analysis. Since this region is very close to the limb where the stray light does not significantly contribute to the line profile, no stray light correction is implemented to the EIS or SUMER data.
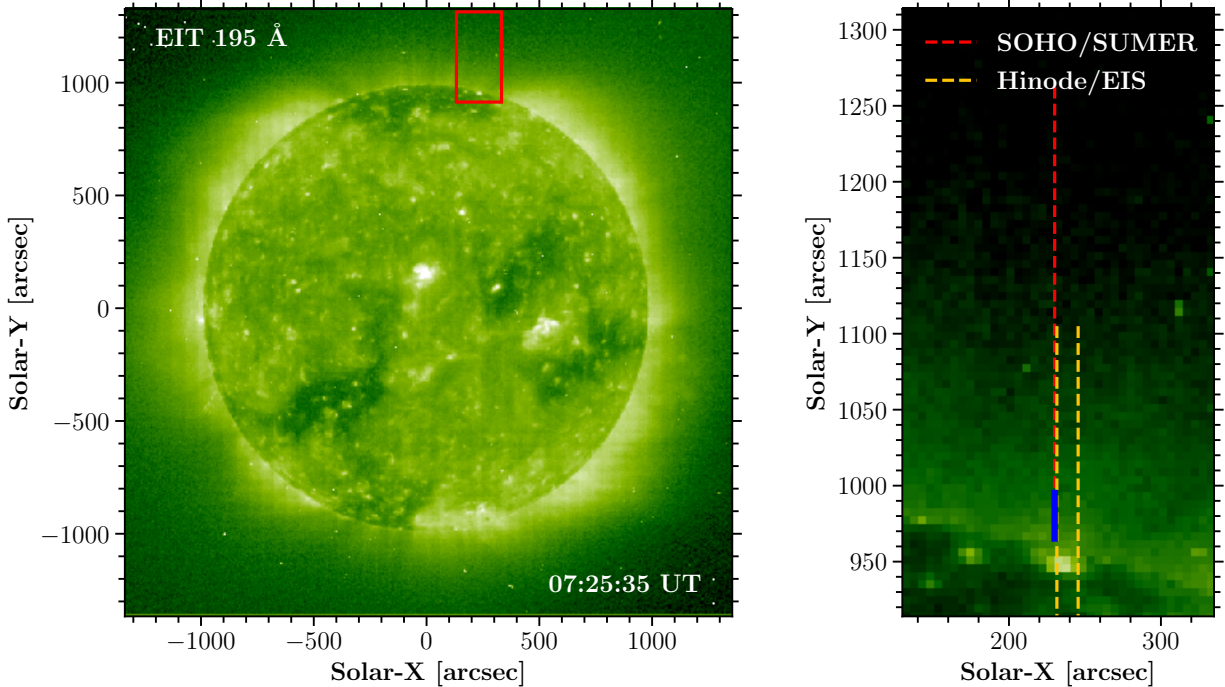
Figure 1. Positions of SUMER and EIS slits on the EIT 195 context image. **Left**: EIT 195 image of the full solar disk on 2007 November 16 at 07:25:35 UT. The red rectangle displays the FOV of the right panel. **Right**: Slit pointing at the coronal hole boundary. The red dashed line shows the location of the 300″ slit of SUMER. The yellow dashed lines show the first and the last pointing location of the EIS slit during the seven-step raster. The blue solid line shows the region of the data analyzed in this paper. Link to the `Jupyter` notebook creating this figure: ⟳.

2.2. *Data Fitting*

We performed the single/multi-Gaussian fitting to the unblended/blended spectral lines, respectively. The spectrum is fitted by a constant background I_{bg} plus a single Gaussian profile or multiple Gaussian profiles, where the profile of each line is described by the total intensity $I_{\mathrm{tot},i}$, the wavelength of the line centroid $\lambda_{0,i}$, and the full width at half maximum (FWHM) $\Delta\lambda_i$, i.e., the fitting model I_{model} can be written as:

$$I_{\mathrm{model}}(\lambda) = \sqrt{\frac{4\ln 2}{\pi}} \sum_{i=1}^{m} \frac{I_{\mathrm{tot},i}}{\Delta\lambda_i} \exp\left[-\frac{(\lambda - \lambda_{0,i})^2}{\Delta\lambda_i^2/4\ln 2}\right] + I_{\mathrm{bg}}$$

(3)

where m is the total number of spectral lines to be fitted. For complicated blended spectral lines, we performed simple minimum χ^2 fitting using the SciPy `curve_fit` function. The χ^2 is

$$\chi^2 = \sum_{j=1}^{n} \frac{[I_{\mathrm{obs}}(\lambda_j) - I_{\mathrm{model}}(\lambda_j)]^2}{\sigma_I^2(\lambda_j)}$$

(4)

where n is the number of fitted wavelength points, λ_j is the wavelength of the $j-$th wavelength point, $I_{\mathrm{obs}}(\lambda_j)$ is the observed intensity at λ_j), and $\sigma_I(\lambda_j)$ is the uncertainty of the observed intensity. The 1σ uncertainties

of the fitting parameters are given by the square root of the diagonal of the covariance matrix.

To give a better estimate of the fitting uncertainty in the single Gaussian fitting, we adopted Monte Carlo analysis (Hahn et al. 2012) in the following steps: (1) we fit the unblended spectral line by simple χ^2 minimization using the original uncertainty. (2) we re-assigned the uncertainty of the intensity σ_I to be the larger of either the fitting residual or the original uncertainty. (3) we added noise to the observed intensities generated from a normal distribution $\mathcal{N}(\mu = 0, \sigma^2 = \sigma_I^2)$ and then fit the spectrum with additional noise. (4) we repeated step (3) 10,000 times and determined the uncertainty by calculating the standard deviations of the fitting results.

To subtract the EIS instrumental broadening, we used the Gaussian instrumental width $\Delta\lambda_{\mathrm{inst}}$ given by the IDL routine `eis_slit_width` and removed it by:

$$\Delta\lambda_{\mathrm{true}} = \left(\Delta\lambda_{\mathrm{fit}}^2 - \Delta\lambda_{\mathrm{inst}}^2\right)^{1/2}$$

(5)

where $\Delta\lambda_{\mathrm{fit}}$ is the fitted FWHM. The instrumental width $\Delta\lambda_{\mathrm{inst}}$ of SUMER is removed directly by the IDL routine `con_width_funct_4`. The uncertainty of the true line width is propagated by

$$\sigma_{\Delta\lambda_{\mathrm{true}}} = \left|\frac{\partial\Delta\lambda_{\mathrm{true}}}{\partial\Delta\lambda_{\mathrm{fit}}}\right|\sigma_{\Delta\lambda_{\mathrm{fit}}} = \frac{\Delta\lambda_{\mathrm{fit}}}{\Delta\lambda_{\mathrm{true}}}\sigma_{\Delta\lambda_{\mathrm{fit}}}$$

(6)

2.3. Ion Temperature Estimation

The information about ion temperatures in the solar corona is embedded in spectral line widths $\Delta\lambda_{\mathrm{true}}$:

$$\Delta\lambda_{\mathrm{true}} = \left[4\ln 2 \left(\frac{\lambda_0}{c} \right)^2 \left(\frac{2k_B T_i}{m_i} + \xi^2 \right) \right]^{1/2} \quad (7)$$

where c is the speed of light, k_B is the Boltzmann constant, T_i stands for the LOS ion temperature, m_i is the mass of the ion, ξ is the nonthermal velocity. In observations, ξ might be contributed by the propagation of Alfvén waves and other unresolved bulk motion along the LOS. As λ_0 is well determined, we can obtain the effective LOS velocity v_{eff} from the width of each fitted spectral line:

$$v_{\mathrm{eff}} = \left(\frac{2k_B T_i}{m_i} + \xi^2 \right)^{1/2} \quad (8)$$

The effective velocities v_{eff} of lines of the same ion should be identical unless the lines of the same ion have very different excitation energies, which might cause the lines to form at different positions along the LOS. Therefore, to use multiple fitted lines from the same ion, we derived the weighted average $\bar{v}_{\mathrm{eff}}$ (See Appendix A) of the effective velocity v_{eff} from spectral lines that have small fitting uncertainties and high S/N.

We estimate the limits of ion temperatures T_i from effective velocities $\bar{v}_{\mathrm{eff}}$ using the method proposed by Tu et al. (1998). This method only assumes that the nonthermal velocity ξ is the same for all ions so that we can estimate both an upper and a lower limit to the ion temperature. To estimate the upper limit, we simply assumed that the lines are dominated by thermal broadening, i.e., $\xi = 0$, therefore

$$T_{i,\mathrm{max}} = \frac{m_i}{2k_B} \bar{v}_{\mathrm{eff}}^2 \quad (9)$$

To obtain the lower limit $T_{i,\mathrm{min}}$, we first set the upper limit of the nonthermal velocity ξ_{max} to be equal to the smallest effective velocity $\bar{v}_{\mathrm{eff}}$ among all lines. Then we removed ξ_{max} from all $\bar{v}_{\mathrm{eff}}$ to calculate $T_{i,\mathrm{min}}$:

$$T_{i,\mathrm{min}} = \frac{m_i}{2k_B} \left(\bar{v}_{\mathrm{eff}}^2 - \xi_{\mathrm{max}}^2 \right) \quad (10)$$

We note that the interval $[T_{i,\mathrm{min}}, T_{i,\mathrm{max}}]$ should not be interpreted as an uncertainty but as a range of equally likely values. On the other hand, we propagated the uncertainty in the average effective velocity $\bar{v}_{\mathrm{eff}}$ to the uncertainty of each $T_{i,\mathrm{max}}$ and $T_{i,\mathrm{min}}$.

2.4. Electron Density and Temperature Diagnostics

We measured the electron density n_e and temperature T_e at the coronal hole boundary using the intensity ratios of two emission lines of the same ion. These lines are listed in Tables 1 and 2. This approach assumed that the plasma along the LOS is nearly homogeneous in density and isothermal. We used the latest CHIANTI 10 atomic database to calculate plasma emissivities at different electron densities and temperatures.

Apart from the fitting uncertainty, the radiometric calibration might also affect the precision of the electron density and temperature diagnostics. The SUMER radiometric calibration has absolute uncertainties of 33% in detector A and 36% in detector B (Pauluhn et al. 2001) after the SOHO recovery in 1998. Although the relative ratios of two lines might have a smaller uncertainty, we conservatively use those values. EIS has two competing in-flight radiometric corrections to the laboratory calibration proposed by Del Zanna (2013, GDZ) and Warren et al. (2014, HPW). The two methods show different detector responses across the SW and LW detectors, as well as their wavelength dependence. We show the two different correction factors versus wavelength, as well as the locations of the spectral lines used for diagnostics in Figure 2. In general, the two methods show similar variations of correction factors versus wavelength, but GDZ gives more small bumps in the curve. For example, the increase in the GDZ correction factor around 188 Å makes the Fe VIII 185.213/186.598 Å ratio 10% smaller than the HPW ratio.

To estimate the uncertainty caused by the LOS structures and the radiometry, we performed electron density and temperature diagnostics using intensity ratios of two (or multiple if self-blended) spectral lines. We applied the GDZ and HPW corrections to the EIS data to further investigate the differences between the two methods.

2.5. AWSoM-R Simulation

The synthetic data presented in this paper is the result of a simulation ran with the Space Weather Modeling Framework (SWMF, Tóth et al. 2012) Alfvén Wave Solar Model - realtime (AWSoM-R, Sokolov et al. 2021) model combined with the post-processing tool SPECTRUM (Szente et al. 2019), which is also part of the SWMF. AWSoM-R is a version of the Alvén Wave Solar atmosphere Model (AWSoM, van der Holst et al. 2014) model with the change of handling the transition region: instead of using the artificial grid stretching (Li-

Table 1. Spectral lines ratios used for electron density diagnostics.

Ion	$\log T_{\max}$ [K]	Wavelength [Å]	Instrument
Fe VIII	5.75	185.213/186.598	EIS
Mg VII	5.80	276.154/280.742	EIS
Fe IX	5.85	189.935/191.206	EIS
Mg IX	5.95	694.006/706.060	SUMER
Si X	6.00	258.374/261.056	EIS
Fe XI	6.00	182.167/(188.216+188.299)	EIS
Fe XII	6.05	(186.854+186.887)/195.119	EIS

NOTE—$T_{\max}$ is the temperature of the maximum line formation calculated by CHIANTI using the DEM derived from the average coronal hole spectra in Vernazza & Reeves (1978)

.

Table 2. Spectral lines ratios used for electron temperature diagnostics.

Ion	$\log T_{\max}$ [K]	Wavelength [Å]	Instrument
Fe VIII	5.75	185.213/253.956	EIS
Fe IX	5.85	191.206/197.854	EIS
Fe X	5.95	174.531/(257.259+257.261)	EIS
Fe X	5.95	177.240/(257.259+257.261)	EIS
Fe X	5.95	184.537/(257.259+257.261)	EIS
Mg IX	5.95	706.060/749.552	SUMER
Fe XI	6.00	(188.216+188.299)/(257.547+257.554)	EIS

NOTE—$T_{\max}$ is the temperature of the maximum line formation calculated by CHIANTI using the DEM derived from the average coronal hole spectra in Vernazza & Reeves (1978).

onello et al. 2001), this implementation of the model uses the magnetic field lines of the potential field source surface model to bridge the AWSoM model starting at $1.05\,R_\odot$ to the chromosphere through the transition region. The equations of AWSoM-R are solved along the 1D fieldlines between $1\,R_\odot$ and $1.05\,R_\odot$. This removes the high-resolution part of AWSoM, resulting in faster than the real-time model. More importantly, it provides synthetic data of the low corona without the effects of the transition-region stretching. We ran the simulation using the magnetogram from the Global Oscillation Network Group (GONG, Harvey et al. 1996) of 2007-11-04UT09:59:00 for 200,000 steps and extracted data corresponding to the LOS of the region observed by EIS and SUMER. To confirm the accuracy of the modeled corona and solar wind, we compared the plasma speed, density, temperature, and magnetic field strength with

observations in the inner heliosphere in Figure 3, which gave a reasonable comparison at 1 AU.

We then synthesized the UV spectral line profiles from the AWSoM-R simulation results using the SPECTRUM module (Szente et al. 2019), which calculates the emissivity profiles voxel by voxel and integrates them along the LOS. In each voxel, the SPECTRUM module calculates the Doppler shift, and thermal and nonthermal broadening of the emissivity profile. The FWHM of the emissivity profile is

$$\Delta\lambda = \left[4\ln 2\left(\frac{\lambda_0}{c}\right)^2\left(\frac{2k_B T_p}{m_p A_i} + \xi_w^2\right)\right]^{1/2} \quad (11)$$

where m_p is the proton mass, A_i is the mass number of the ion. As AWSoM-R does not model heavy ion species, we used the proton temperature T_p to calculate the thermal broadening of heavy ions. The wave-
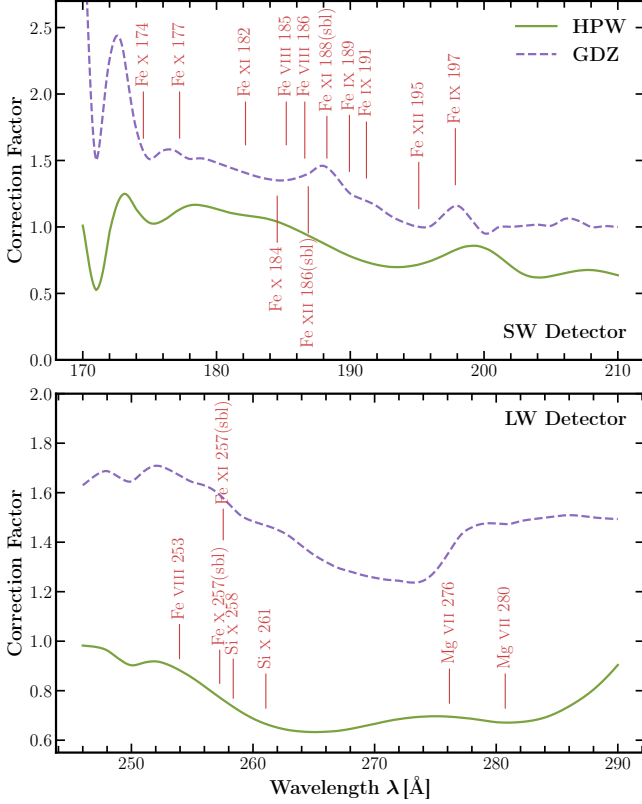
Figure 2. Two in-flight radiometric correction factors in the SW (**top**) and LW (**bottom**) detectors of EIS. Locations of the spectral lines used for electron temperature and density diagnostics are displayed as well. Link to the `Jupyter` notebook creating this figure ⟳.

induced nonthermal component ξ_w is

$$\xi_w^2 = \frac{1}{2}\langle \delta u^2 \rangle \sin^2 \alpha = \frac{1}{2}\frac{\omega^+ + \omega^-}{\rho} \sin^2 \alpha = \frac{1}{8}\left(z_+^2 + z_-^2\right)\sin^2 \alpha. \quad (12)$$

where α is the angle between the direction of the local magnetic field and the LOS, $z_{\pm}$ are the Elsässer variables for forward- and backward-propagating waves and the respective energy densities are $\omega_{\pm}$. We refer to Szente et al. (2019) for more details about the SPECTRUM module.

3. RESULTS

3.1. Observations

3.1.1. Line Fitting and Average Effective Velocity

Figure 4 displays the single-Gaussian fitting of the Na IX 681 Å line observed by SUMER. The line wings resolved by SUMER are well-fitted by the Gaussian function. On the other hand, the peak intensity of the observed line core is larger than the best-fit line profile. A multi-Gaussian fitting example of several spectral lines

around 192 Å observed by EIS is shown in Figure 5. Although the Fe XII 192.394 Å line is blended with some other unidentified lines on the blue wing, we can still get a proper fitting of line widths. Note that the reduced χ^2 function in both examples is less than one, which might indicate the Poisson statics or propagation of errors overestimates the uncertainty. The EIS and SUMER line widths used for ion temperature diagnostics are listed in Table C1.

Then we derived the average effective velocity for ions, which have multiple spectral lines observed by the same instrument. Spectral lines from the same ion but observed by different instruments are treated separately for comparison (e.g., the O VI 184 Å line observed by EIS and the O VI 1032, 1037 Å lines observed by SUMER). Figure 6 shows the effective velocity of Fe XII 192.394, 193.509, and 195.119 Å triplet lines and the average effective velocity $\bar{v}_{\mathrm{eff}}$. The Fe XII 192 Å line width shows greater uncertainty, as it is weaker than the other two lines of the triplet and the blending. The Fe XII 195 Å line is slightly broader than the 192 Å and 193 Å lines by $\sim 5\,\mathrm{km\,s^{-1}}$, which could be related to the instrumental effect (Del Zanna et al. 2019) and the blended Fe XII 195.179 Å line (Young et al. 2009). The average effective velocity of Fe XII with 1σ uncertainty is $40.6^{+1.8}_{-1.9}\,\mathrm{km\,s^{-1}}$. The average effective velocities of all the ions used in the following study are listed in Table C1.

3.1.2. Electron Density and Temperature Diagnostics

Before determining the ion temperatures from the spectral line widths, we first measured the electron density and temperature using the intensity ratios listed in Table 1 and 2. We corrected the EIS intensity ratios using the GDZ or HPW method, except for the Fe IX 189/191 Å ratio, because the two lines are very close to each other. The Mg IX 706 Å line observed by SUMER is located at the boundary of the coated and bare part of the detector. Although the KBr and bare responsivities at ~ 700 Å are very similar, we still measured the electron density and temperature assuming that the entire Mg IX 706 Å line is recorded in the KBr or bare parts. Figure 7 summarizes the measurements of the electron density and temperature, where the ions are ordered by their formation temperature. Electron density measurements range from $\log n_e \sim 7.7$ to $\log n_e \sim 9.0$, depending on line ratios and calibration methods. The measured electron density increases with the maximum formation temperature of the ion. The electron density measured from cooler line pairs like Fe VIII 185/186 Å and Mg VII 276/280 Å is around $\log n_e \sim 8.0$. The hotter Fe IX 189/191 Å and Mg IX 694/706 Å ratios give the electron density $\log n_e \sim 8.5$. The highest electron
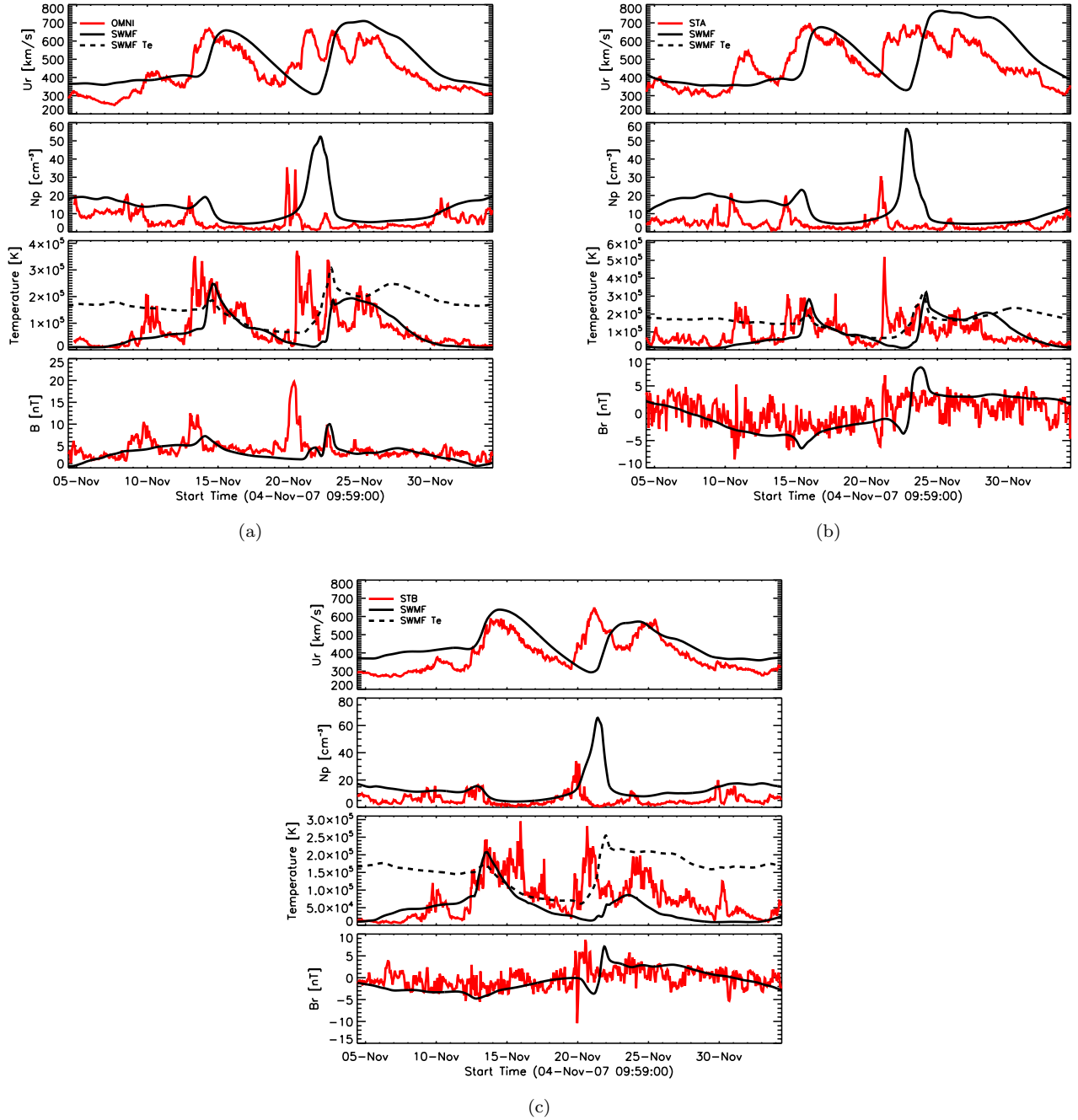
(a)

(b)

(c)

Figure 3. AWSoM-R simulation results compared to in-situ measurements provided by OMNI (a) and STEREO spacecrafts (b and c). Red shows observational data, black is synthetic data with AWSoM-R. Each figure shows from top to bottom the velocity, density, temperature and magnetic field data comparisons.

density $\log n_e \sim 8.7 - 9.0$ is measured from the hottest Si x 258/261 Å, Fe xi 182/188 Å, and Fe xii 186/195 Å lines.

We chose two electron densities $\log n_e = 8.0$ and $\log n_e = 8.5$ to calculate temperature-sensitive line ratios using CHIANTI. The inferred electron temperatures from different line ratios are shown in the right panel of Figure 7. The color data points represent T_e measured

at $\log n_e = 8.0$ and the grey ones are T_e measured at $\log n_e = 8.5$. Most electron temperatures range from $\log T_e \sim 5.9$ to $\log T_e \sim 6.2$. EIS electron temperatures show a wider distribution due to different radiometric calibrations. In general, EIS electron temperatures measured from HPW line ratios are higher than GDZ electron temperatures by 0.1 to 0.3 dex (a factor of 1.3 to 2.0 on the linear scale). Electron temperatures
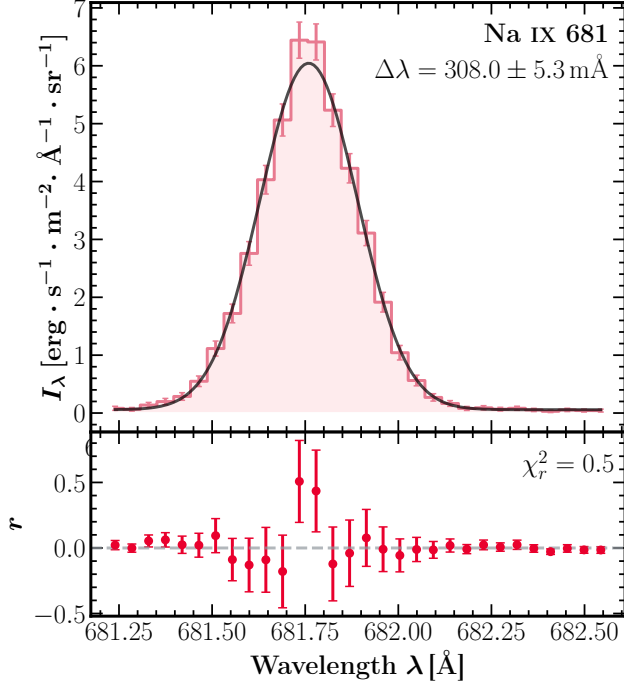
Figure 4. An example of the single-Gaussian fitting of the Na IX 681 Å line observed by SUMER. The top panel shows the observed spectra (step line) and the fitting line profile (black solid line). The lower panel displays the fitting residual. Link to the `Jupyter` notebook creating this figure ⟳.
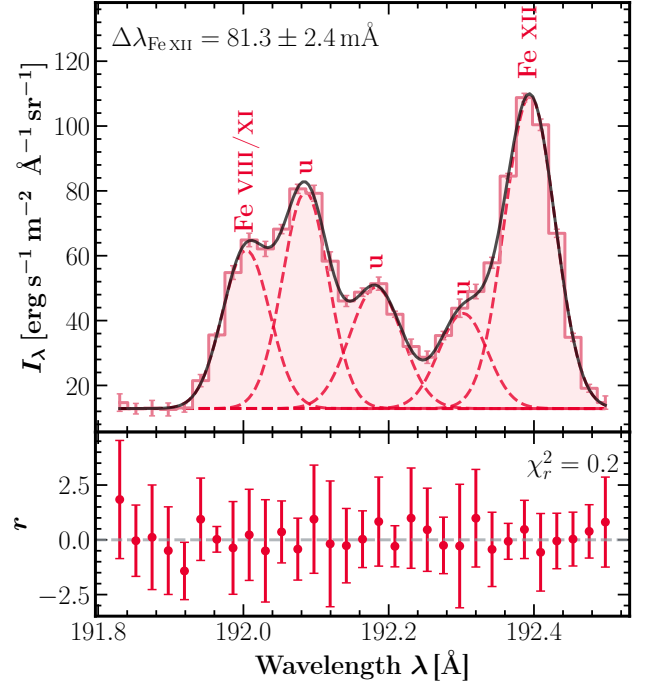
Figure 5. An example of the multi-Gaussian fitting of the blended lines near 192 Å observed by EIS, including the blended Fe VIII and Fe XI 192.021 Å, Fe XII 192.394 Å, and three other unidentified (u) lines. **Top**: Observed spectrum (step curve with error bars), fitted spectrum I_{model} (black solid line), and individual Gaussian components (red dashed line). **Bottom**: residual of the fitting. Link to the `Jupyter` notebook creating this figure: ⟳.

measured from hotter line pairs like Fe X and XI are slightly larger than those inferred from cooler line ratios like Fe VIII. Although the Fe IX 191/197 Å ratio is less affected by the cross-calibration between two detectors, the line ratio is more sensitive to the electron density. We measured higher electron temperatures in the Fe X 184/257 Å ratio than the other two Fe X 174/257 Å and 177/257 Å ratios. As the magnetic field in the coronal hole is very weak, the blended Fe X 257 Å magnetic induced transition (MIT) should not affect the Fe X line ratios. The electron temperature inferred from the Mg IX 706/749 Å ratio lies between most of the HPW and GDZ electron temperatures. Finally, we somewhat arbitrarily chose $\log T_e = 5.9$ to $\log T_e = 6.15$ as the electron temperature of the LOS plasma to cover most of the measured electron temperatures.

3.1.3. Ion Temperature Diagnostics

Figure 8 shows the minimum and maximum of the ion temperature $T_{i,\mathrm{min}}$ and $T_{i,\mathrm{max}}$ versus the ion charge-to-mass ratio (Z/A) of the ion, along with the electron temperature T_e determined in Figure 7. The values of $T_{i,\mathrm{min}}$ and $T_{i,\mathrm{max}}$ are also listed in Table C1. We measured the ion temperature of ions with Z/A ranging from 0.125 (Fe VIII) to 0.37 (Mg X). Since the coronal hole

plasma is cooler than the plasma in quiet Sun or active regions, spectral lines from higher charge states are too weak to identify or fit. The narrowest lines are Fe VIII observed by EIS and Si X observed by SUMER, with an effective velocity $v_{\mathrm{eff}} \sim 32\,\mathrm{km\,s^{-1}}$, which is treated as the maximum nonthermal velocity ξ_{max}. Note that the Si X 624.694 Å line observed by SUMER is blended with the stronger Mg X 624.941 Å line so the uncertainty of effective velocity is quite large.

The measured ion temperatures T_i show a U-shaped dependence on the charge-to-mass ratio Z/A where the U-shaped valley locates at $0.2 \leq Z/A \leq 0.33$. These results are similar to the ion temperatures measured by Landi & Cranmer (2009) at the center of the coronal hole using SUMER lines. Ions with $0.12 \leq Z/A \leq 0.19$, except for the two ions Fe VIII and Fe IX with the smallest v_{eff}, show ion temperatures much higher than the local electron temperature T_e. The SUMER ion temperatures for $0.12 \leq Z/A \leq 0.19$ are above $\log T_i \sim 6.5$. The ion temperature T_i decreases roughly with Z/A between 0.19 and 0.25, then shows a plateau that overlaps the local electron temperature T_e ranging from $Z/A = 0.25$
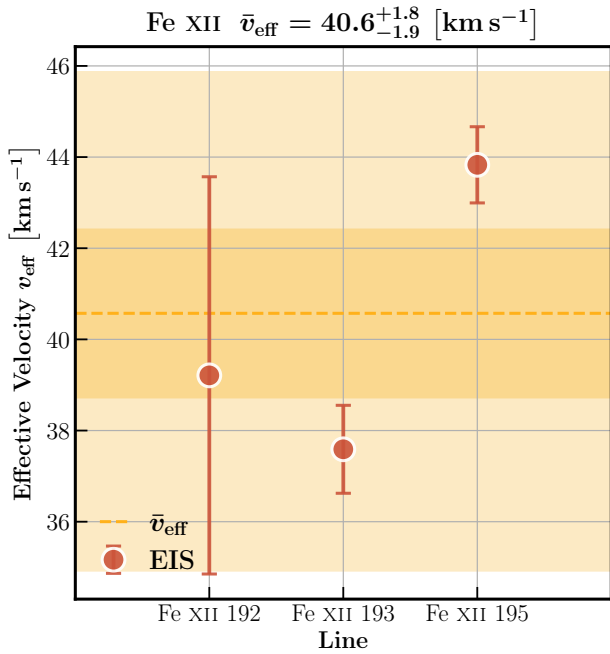
Fe XII $\bar{v}_{\mathrm{eff}} = 40.6^{+1.8}_{-1.9}$ $\left[\mathrm{km\,s^{-1}}\right]$

Figure 6. The measured effective velocity v_{eff} of the Fe XII 192, 193, and 195 Å lines and the average effective velocity $\bar{v}_{\mathrm{eff}}$ of Fe XII. The horizontal dashed line indicates the average effective velocity $\bar{v}_{\mathrm{eff}}$. The darker/lighter shaded regions indicate the $1\sigma/3\sigma$ uncertainty level respectively. Link to the `Jupyter` notebook creating this figure: ⟳.

to 0.33. Above $Z/A = 0.33$, the ion temperature T_i becomes greater than the local electron temperature T_e again. Mg X with the largest $Z/A = 0.37$ reveals a lower ion temperature T_i than the other ions with $Z/A > 0.33$ (Mg IX, Ne VIII and Na IX).

The ion temperature diagnostics might be affected by the formation electron temperature of the ion. For example, some cooler ions observed by EIS, like Mg VI, Mg VII, and O VI, do have lower ion temperatures compared to the hotter ions like Fe XII and Fe XIII. On the other hand, the ion temperatures of the different Fe charge states observed by EIS (Fe VIII to XIII) and Mg charge states (Mg VIII to Mg X) observed by SUMER do not monotonically increase with charge states (formation temperature). We further investigate the influence of the ion formation temperature and bulk motions along the LOS in the AWSoM-R simulation (see Section 3.2).

We expected that the spectral lines from the same ion would have shown similar effective velocities v_{eff} across the SUMER and EIS observations if the instrumental broadening was removed correctly. However, in most cases, the effective velocity v_{eff} and the ion temperature T_i measured by SUMER are greater than v_{eff} and T_i of the same ion measured

by EIS when the instrumental broadening is removed by SolarSoft routines `eis_slit_width.pro` (EIS) and `con_width_funct_4.pro` (SUMER). The only exception is Si X, which also might be due to the large fitting uncertainty caused by line blending. The most reliable comparisons between EIS and SUMER line widths are Fe VIII and O VI because both EIS and SUMER record strong emission lines from these ions. The effective velocity $v_{\mathrm{eff}} = 50.2 \pm 7.5\,\mathrm{km\,s^{-1}}$ of Fe VIII measured from SUMER is 30% to 50% higher than that measured by EIS of $v_{\mathrm{eff}} = 32.2^{+1.8}_{-1.9}\,\mathrm{km\,s^{-1}}$. And the O VI $v_{\mathrm{eff}} = 50.6 \pm 0.6\,\mathrm{km\,s^{-1}}$ observed by SUMER is also about 25% larger than $v_{\mathrm{eff}} = 40.6 \pm 2.3\,\mathrm{km\,s^{-1}}$ found in the EIS spectrum. We will further discuss the uncertainty caused by instrumental broadening in Section 4.1.

3.2. *Simulations*

Figure 9 shows the physical parameters in the AWSoM-R simulation. The coronal hole boundary region in the simulation does not show complicated structures along the LOS, except for a streamer in the electron and proton temperature plots. The electron temperature T_e in the studied region is ~ 1 MK, and the electron density n_e is $\sim 10^8\,\mathrm{cm^{-3}}$, which matches the results of the T_e and n_e diagnostics in Section 3.1.2. The LOS velocity varies from 0 to $\pm 20\mathrm{km\,s^{-1}}$ where most spectral lines form in the studied region. The wave-induced nonthermal velocity ξ is about $20\,\mathrm{km\,s^{-1}}$ in the open field lines between 1.01 to $1.04\,R_\odot$. The maximum formation temperature T_{max} of the spectral line affects the line formation region along the LOS. For example, most photons of the Fe VIII 186 Å, a cooler line that forms at $\log T_{\mathrm{max}} \sim 5.75$, are emitted by the plasma from $-0.3\,R_\odot$ to $0.3\,R_\odot$ along the LOS. Most of the hotter Fe XII 192 Å ($\log T_{\mathrm{max}} \sim 6.05$) emission forms from the plasma between $-0.5\,R_\odot$ and $0.5\,R_\odot$.

To evaluate how LOS bulk motions influence the spectral line profiles, we synthesized Fe VIII 186 Å and Fe XII 192 Å profiles either with or without the Doppler effect in Figure 10. The cooler Fe VIII 186 Å line is less affected by the integration of bulk motions along the LOS. The macroscopic Doppler broadening caused by v_{LOS} increases the line width only by about 2.5% and becomes even more negligible when the profile is convolved with the instrumental width and degraded to EIS spectral resolution. The true width of the hotter Fe XII 192 Å line that forms in an extensive region along the LOS increases from 38.0 Å to 47.3 Å due to the macroscopic Doppler broadening. After convolving with the instrumental widths, the bulk motion along the LOS still increases the Fe XII 192 Å line width from 81.3 Å to
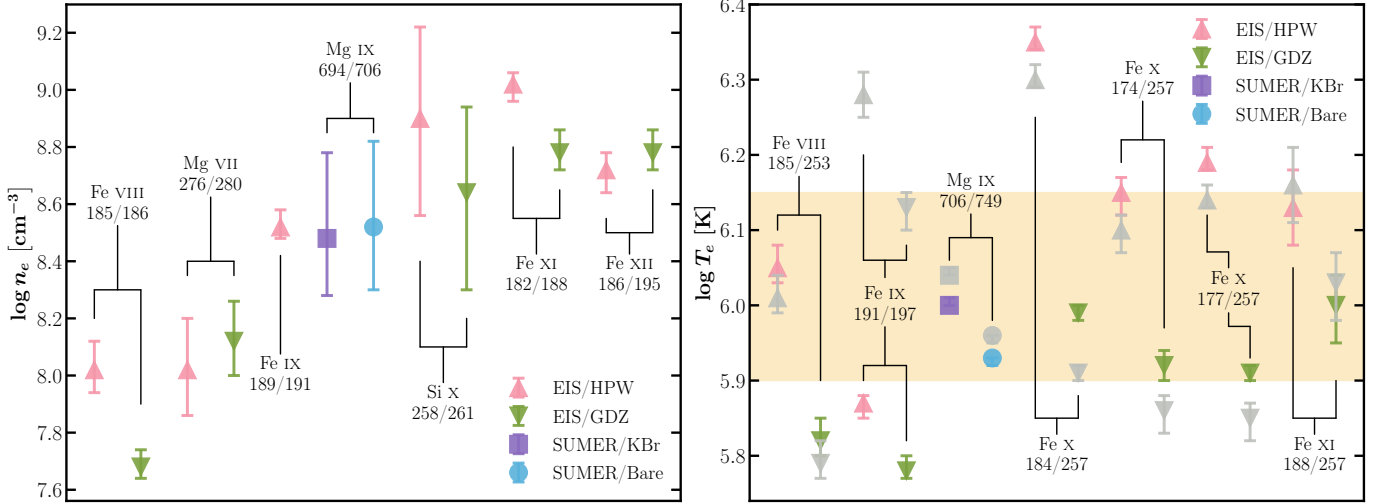
Figure 7. Left: Electron density n_e diagnostics of the coronal hole boundary region shown in Figure 1. **Right:** Electron temperature T_e diagnostics in the same region. The electron density and temperature are measured by intensity ratios of EUV spectral lines. For diagnostics using EIS data, the intensity ratios are corrected by either the HPW or GDZ method (except for the unaffected Fe IX 189/191 ratio). The Mg IX 706 Å line locates at the boundary between the KBr-coated and bare part of the SUMER detector. Therefore we show both results assuming that the entire Mg IX 706 Å is either in the coated or bare part. The colored data points in the right panel represent T_e at $\log n_e = 8.0$, while the grey ones stand for T_e inferred at $\log n_e = 8.5$. The yellow shaded area displays the chosen range of the electron temperature. The line ratios are sorted from left to right by the maximum formation temperature $T_{\max}$. Link to the Jupyter notebook creating this figure 🪐.
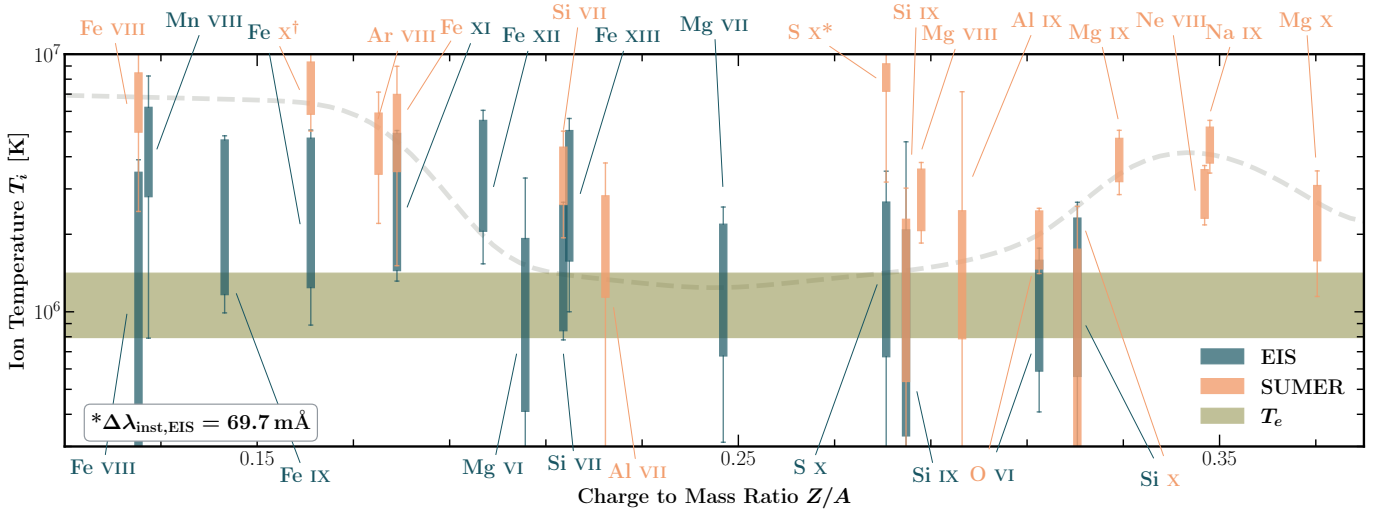
Figure 8. Estimated ion temperatures T_i vs. ion charge to mass ratio Z/A. Note that this plot is not the typical box plot to show the data distributions. The boxes show possible ion temperature intervals between $T_{i,\min}$ and $T_{i,\max}$. The whiskers indicate the uncertainty in $T_{i,\min}$ and $T_{i,\max}$. The ion temperatures inferred from lines observed by either EIS or SUMER are shown in dark green and orange, respectively. The horizontal shaded area displays the electron temperature measurement shown in Figure 7. The gray dashed line is arbitrarily drawn to illustrate the U-shaped dependence. * The S X 776.373 Å line is poorly fitted. † The Fe X 1028 Å line is self-blended, but still kept for comparison. Link to the Jupyter notebook creating this figure 🪐.

85.2 Å, which is beyond the fitting uncertainty in real observations.

Figure 11 compares the observed line widths with the synthetic line widths. We note that the SPECTRUM module uses the proton temperature T_p as an approximation of the ion temperature T_i to calculate the ther-

mal broadening. Therefore, the excessive observed line widths might indicate additional heating to the heavy ions compared to the protons. Most of the spectral lines observed by SUMER show widths similar to or larger than those of the synthetic lines, while most of the EIS lines are $\sim 5 - 10\,\mathrm{km\,s^{-1}}$ narrower than the synthetic
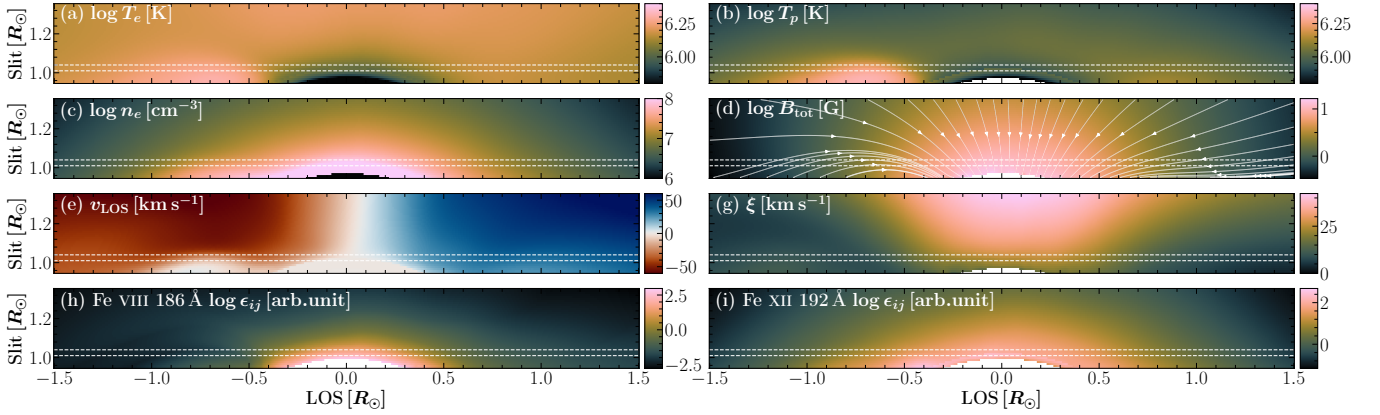
Figure 9. Physical parameters in the AWSoM-R simulation box located at the polar coronal hole boundary: **(a)** Electron temperature T_e, **(b)** Proton temperature T_p, **(c)** Electron density n_e, **(d)** Total magnetic field B_{tot} and field lines, **(e)** LOS velocity v_{LOS}, **(g)** Wave-induced nonthermal velocity ξ_w, **(h)** Emissivity of the Fe VIII 186 Å line, **(i)** Emissivity of the Fe XII 192 Å line. The white dotted lines show the region corresponding to the observation. Link to the `Jupyter` notebook creating this figure ⟳.
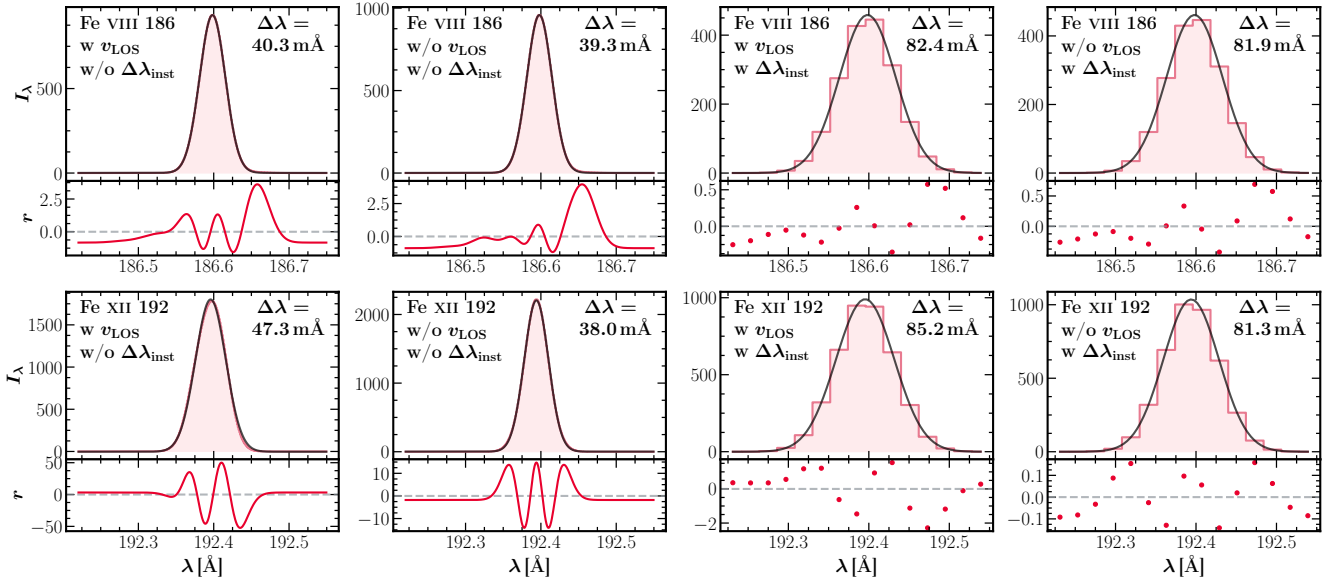
Figure 10. Fitting synthetic Fe VIII 186 Å and Fe XII 192 Å lines under different conditions. w v_{LOS}: Synthetic profiles with the Doppler effect. w/o v_{LOS}: Synthetic profiles without the Doppler effect. w $\Delta\lambda_{inst}$: Synthetic profiles convolved with instrumental width $\Delta\lambda_{inst} = 70$ mÅ and rebinned to EIS spectral resolution. w/o $\Delta\lambda_{inst}$: Synthetic profiles without instrumental effects. Link to the `Jupyter` notebook creating this figure ⟳.

lines. The differences between the SUMER and synthetic line widths show a similar U-shaped dependence of Z/A. The SUMER lines with $0.12 \leq Z/A \leq 0.21$ are wider than the synthetic lines by $\sim 5 - 10$ km s^{-1}. At $0.33 \leq Z/A \leq 0.35$, the SUMER lines show excessive widths of $\sim 10 - 20$ km s^{-1} compared to the simulation. For ions that have spectral lines observed by both EIS and SUMER, AWSoM-R underestimates the SUMER line widths but overestimates the EIS line widths (e.g., Fe VIII, Fe XI, and O VI). This is because the v_{eff} mea-

sured by SUMER is usually greater than v_{eff} of the same ion observed by EIS (also Section 3.1.3). We will discuss

4. DISCUSSION

4.1. *Uncertainty in Instrumental Broadening*

Inconsistency in effective velocity v_{eff} and ion temperature T_i measurements of the spectral lines of the same ion made by SUMER and EIS indicate the uncertainty of the instrumental broadening used in this study. The EIS onboard instrumental widths of the $2''$ slit are measured by searching for the smallest Fe
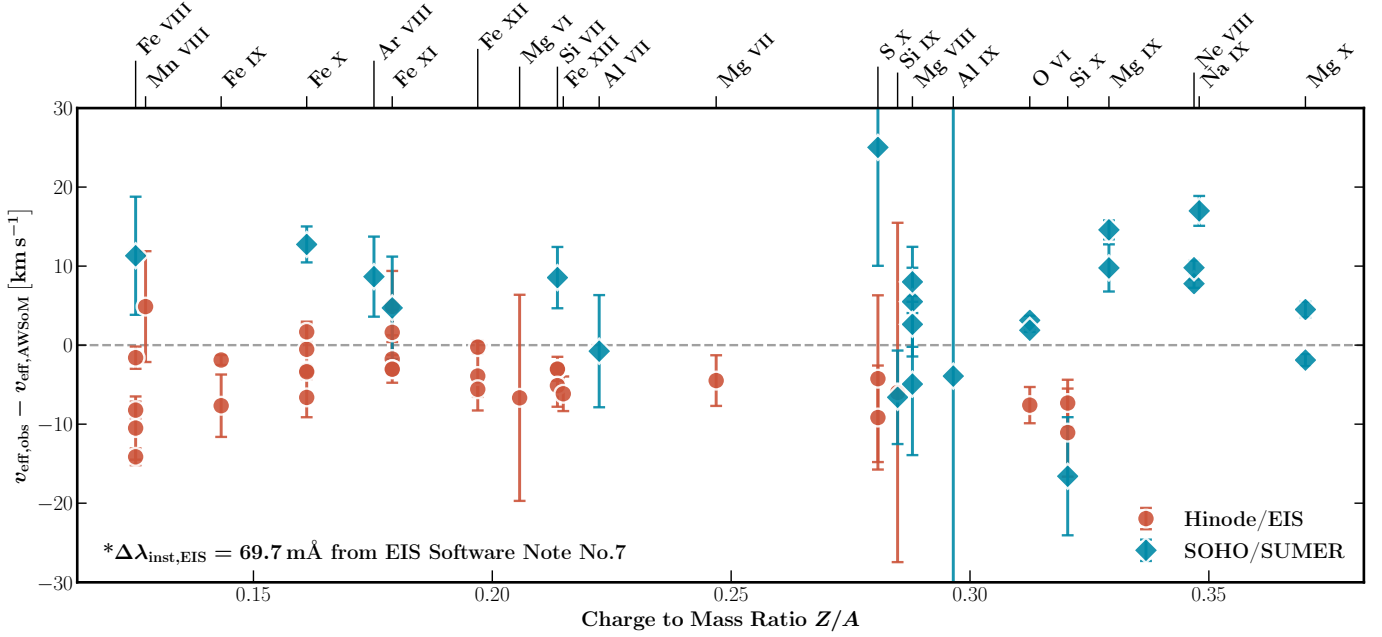
Figure 11. Difference between the observed effective velocity $v_{\mathrm{eff,obs}}$ and the synthetic effective velocity $v_{\mathrm{eff,AWSoM}}$ of each spectral line used in ion temperature diagnostics. Red dots with error bars: EIS lines. Blue diamonds with error bars: SUMER lines. Link to the `Jupyter` notebook creating this figure ⟳.

XII 193.509 Å line widths in a series of off-limb quiet-Sun observations (CALIB_SLIT_SLOT study) and subtracting the thermal widths $\Delta\lambda_{\mathrm{th}} = 23.2$ mÅ assuming $\log T_i = \log T_{\mathrm{max}} = 6.2$ (Young 2011b). This raises concern that the EIS instrumental broadening might be overestimated, as the nonthermal width might be included as the instrumental width in the study. Also, the measured EIS instrumental widths are assumed to only depend on the y-position along the CCD but to be constant across wavelengths. At the averaged 30 pixels, the EIS instrumental width for the 2″ slit is 69.7 mÅ, with an uncertainty of ~ 3 mÅ. The SUMER instrumental widths are calculated based on the measurements of narrow neutral line widths in quiet Sun observations (Chae et al. 1998) and P. Lemaire's calculations of 1997 August 28. The SUMER instrument team chose nine wavelength points at the first order of the grating to determine the wavelength dependence of instrumental widths of detector B.

To investigate the influence of uncertainty in instrumental widths on diagnostic results, we cross-calibrated the EIS instrumental widths $\Delta\lambda_{\mathrm{eff,EIS}}$ with SUMER observations by comparing the O VI 184.117 Å line width observed by EIS and O VI 1031.912 and 1037.613 Å line widths observed by SUMER. We arbitrarily assumed that SUMER gave the correct measurements of line widths, as it measured the cold neutral line widths, where both thermal and nonthermal broadening are negligible to the instrumental broadening. We obtained a

new EIS instrumental width $\Delta\lambda'_{\mathrm{eff,EIS}} = 62.4$ mÅ for the 2″ slit at the averaged 30 pixels, which is about 9% smaller than the original instrumental width $\Delta\lambda_{\mathrm{eff,EIS}} = 69.7$ mÅ and beyond the 3 mÅ uncertainty given by the EIS software note. If the difference between two EIS instrumental widths is caused by the underestimation of the line width to subtract in CALIB_SLIT_SLOT study, we have to subtract an additional width of 28.8 km s^{-1} after the removal of the thermal width to obtain the cross-calibrated width. The possible overestimation of EIS instrumental width at places is also reported in Del Zanna et al. (2019) using an off-limb quiet-Sun observation made on 2006 October 28. In another off-limb quiet-Sun spectra observed on 2007 May 10, Del Zanna et al. (2019) found using a constant EIS instrumental width of 64 mÅ provided Fe XIII 202.044 Å excess widths of 15−20 km s^{-1}, which is similar to previous Skylab and SUMER results.

We performed ion temperature diagnostics with the new EIS instrumental width and show the results in Figure 12. Now the narrowest line width used as the upper limit of nonthermal motion $\xi_{\mathrm{max}} \sim 32$ km s^{-1} is the Si X 624.694 Å line observed by SUMER, which has a relatively larger fitting uncertainty due to the adjacent Mg X 624.941 Å line. It is obvious that the EIS ion temperatures T_i at low Z/A increase significantly and overlap the ranges of the temperature of the same ion observed by SUMER (e.g., Fe VIII and Fe XI). The increase in EIS ion temperatures also makes the U-shaped dependence

on Z/A more prominent, which becomes more similar to the relation between T_i and Z/A in Landi & Cranmer (2009) using a full spectral scan of SUMER. The growth of the Fe XII and Fe XIII temperatures observed by EIS makes them even more different from the ion temperatures of Mg VI, Si VII, and Al VII with similar Z/A between 0.20 and 0.23. This might be due to the macroscopic Doppler broadening of hotter ions found in AWSoM-R simulations (see Sections 3.2 and 4.2).

Figure 13 compares the observed line widths and the synthetic line widths using the cross-calibrated instrumental width of EIS. The widths of the EIS lines increase by $\sim 5 - 10\,\mathrm{km\,s^{-1}}$, which makes the differences between the EIS line widths and the synthetic line widths more consistent with the SUMER's. Now, the EIS lines with $0.12 \leq Z/A \leq 0.19$ are about $0 - 15\,\mathrm{km\,s^{-1}}$ wider than the synthetic lines, whereas the EIS lines for $0.2 \leq Z/A \leq 0.32$ show similar line widths compared to the synthetic ones (within $\pm 5\,\mathrm{km\,s^{-1}}$).

We note that the SUMER instrumental width that we used for cross-calibration also has its own uncertainty. Chae et al. (1998) reported the instrumental width of SUMER detector B with $1''$slit is about 3.0 pixel ($\sim 129\,\mathrm{m\mathring{A}}$ in the first order) with a fluctuation of 0.5 pixel ($\sim 22\,\mathrm{m\mathring{A}}$). This might help explain the inconsistent Mg VIII line widths measured by SUMER. Furthermore, the EIS instrumental broadening might also depend on the wavelength (also see the discussion in Appendix B).

4.2. *Validation of the Technique*

To further validate the ion temperature diagnostics technique, we performed the same diagnostics on the AWSoM-R synthetic line widths. We note that the SPECTRUM module uses the proton temperature T_p to calculate the thermal width $\Delta\lambda_{\mathrm{th}}$ for all spectral lines. Hence, the measured T_i should show no dependence on Z/A. Figure 14 shows the diagnostic results along with the weighted average of the electron temperature $\overline{T}_e$ and the proton temperature $\overline{T}_p$ along the LOS. We used the emissivity ϵ_{ij} of Fe VIII 186 Å and Fe XII 192 Å line as the weights

$$\overline{T} = \frac{\int \epsilon_{ij}(x) T(x)\mathrm{d}x}{\int \epsilon_{ij}(x)\mathrm{d}x} \tag{13}$$

to determine the interval of the weighted average $\overline{T}_e$ and $\overline{T}_p$.

As expected, the measured temperature intervals $[T_{i,\mathrm{min}}, T_{i,\mathrm{max}}]$ do not show U-shaped relations with Z/A and contains the average electron temperature $\bar{T}_e$, because there is no preferential heating in the simulation. Most $T_{i,\mathrm{min}}$ of the synthetic profiles are much lower than the average $\overline{T}_p$ and $\overline{T}_e$ along the LOS, except for the Fe XII and Fe XIII due to bulk motions along the LOS. In

observations, we find that the $T_{i,\mathrm{min}}$ of SUMER ions with $Z/A \leq 0.20$ or $Z/A \geq 0.33$ and EIS ions with $Z/A \leq 0.20$ using $\Delta\lambda'_{\mathrm{eff,EIS}} = 62.4\,\mathrm{m\mathring{A}}$ are greater than the upper limit of the measured T_e, suggesting that they may be preferentially heated compared to local electrons and protons.

4.3. *Non-Gaussian Profiles*

We found that the brightest lines at the coronal hole boundary ($I_{\mathrm{tot}} > 1\,\mathrm{erg\,s^{-1}\,cm^{-2}\,\mathring{A}^{-1}\,sr^{-1}}$) observed by SUMER show non-Gaussian emissions at the line wings, including O VI, Ne VIII, Mg IX, and Mg X lines. The non-Gaussian wings in the plumes and inter-plume regions were reported in early SUMER observations (e.g., Hassler et al. 1997; Wilhelm 1999). Wilhelm (1999) found the presence of non-Gaussian wings in Ne VIII 780 Å profiles in the coronal hole, while they did not find broad non-Gaussian wings in the C III stray light and Ne VIII profiles in closed magnetic field regions. To examine the influence of non-Gaussian wings on the single-Gaussian fitting, we first fitted the non-Gaussian profile by either the Voigt function or a secondary Gaussian component. We found that the double-Gaussian function gives a better fitting of the non-Gaussian wings, also considering that the pressure and natural broadening are negligible in the coronal hole. We also checked the brightest stray light line N IV 765 Å ($I_{\mathrm{tot}} = 0.31\,\mathrm{erg\,s^{-1}\,cm^{-2}\,\mathring{A}^{-1}\,sr^{-1}}$) in this data set, but did not find non-Gaussian wings.

We compared the single-Gaussian and double-Gaussian fitting results of O VI 1032/1037 Å, Ne VIII 770/780 Å, and Mg X 609/624 Å in Figure 15. The single-Gaussian fitting is a good approximation within eight pixels ($\sim \pm 100\,\mathrm{km\,s^{-1}}$) away from the line core but starts to deviate from the observed profiles in the far wings. The secondary Gaussian component provides better fitting up to $\sim \pm 200\,\mathrm{km\,s^{-1}}$, but still leaves some residuals on the red wings of the O VI and Ne VIII doublets.

After removing instrumental broadening, the width of the narrower main component in the double-Gaussian fitting is 10%-40% less than the width obtained in the single-Gaussian fitting, which is equivalent to a reduction of 20%-60% in $T_{i,\mathrm{max}}$. On the other hand, the broader secondary Gaussian component has an effective temperature $2-3$ times greater than the single-Gaussian profile. Since none of these brightest lines is used to estimate the maximum nonthermal velocity ξ_{max}, most $T_{i,\mathrm{min}}$ measurements will not be affected. The width of the secondary Gaussian component is about twice that of the narrower main component for all spectral lines. The intensity ratios of the two components in the same doublets do not agree with each other, let alone
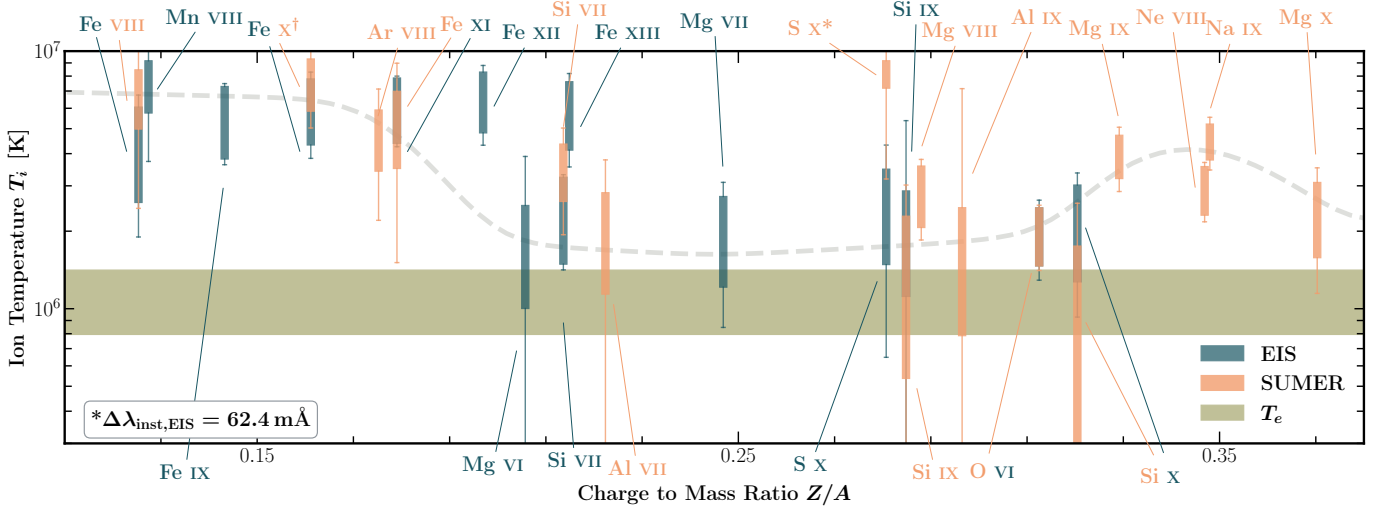
Figure 12. Same as Figure 8 but using cross-calibrated EIS instrumental broadening $\Delta\lambda'_{\rm inst,EIS} = 62.4$ mÅ. The gray dashed line is arbitrarily drawn to illustrate the U-shaped dependence. Link to the `Jupyter` notebook creating this figure ⟳.
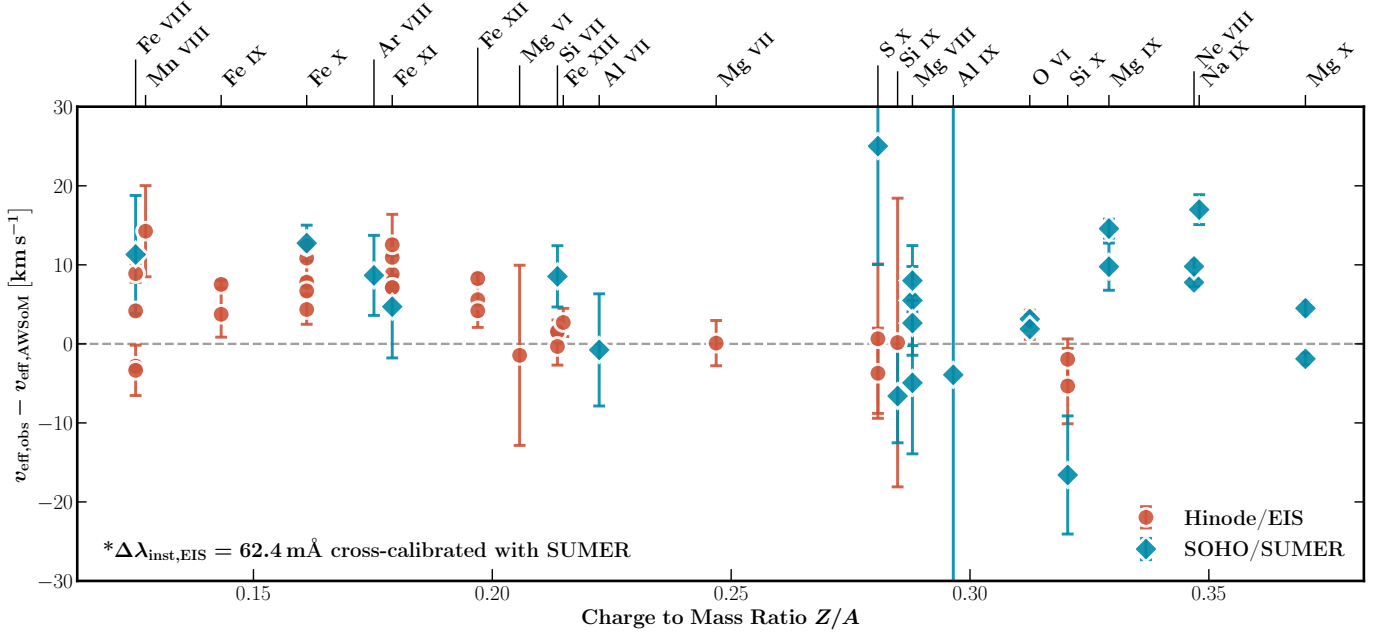

Figure 13. Same as Figure 11 but using EIS instrumental broadening $\Delta\lambda'_{\rm inst,EIS} = 62.4$ mÅ cross-calibrated with SUMER. Link to the `Jupyter` notebook creating this figure ⟳.

with other lines. For example, in O VI 1032 Å and Mg X 609 Å, the secondary component contributes approximately half the intensity of the line profile, while the contribution of the secondary component in O VI 1037 Å and Mg X 624 Å is much less than 50%.

The presence of a secondary Gaussian component in line profiles suggests the existence of high-energy tails in heavy-ion velocity distributions that might influence the ion temperature measurements. However, the inconsistency of intensity ratios of the two Gaussian components raises the question of whether the double-Gaussian fit-

ting is a good approximation to the ion velocity distribution with high-energy tails. The κ distribution, first introduced empirically by (Vasyliunas 1968) and (Olbert 1968), is found to be useful in fitting the suprathermal tails of plasma particles (Lazar et al. 2016). Inspired by Jeffrey et al. (2018) that fitted EIS spectra in the coronal hole assuming a κ distribution, we also attempted fitting these brightest SUMER lines with the κ distribution using the formulae in Dudík & Dzifčáková (2021):

$$I_\kappa(\lambda) = I_0 \left[1 + \frac{(\lambda - \lambda_0)^2}{2(\kappa - 3/2)w_\kappa^2} \right]^{-\kappa} \qquad (14)$$
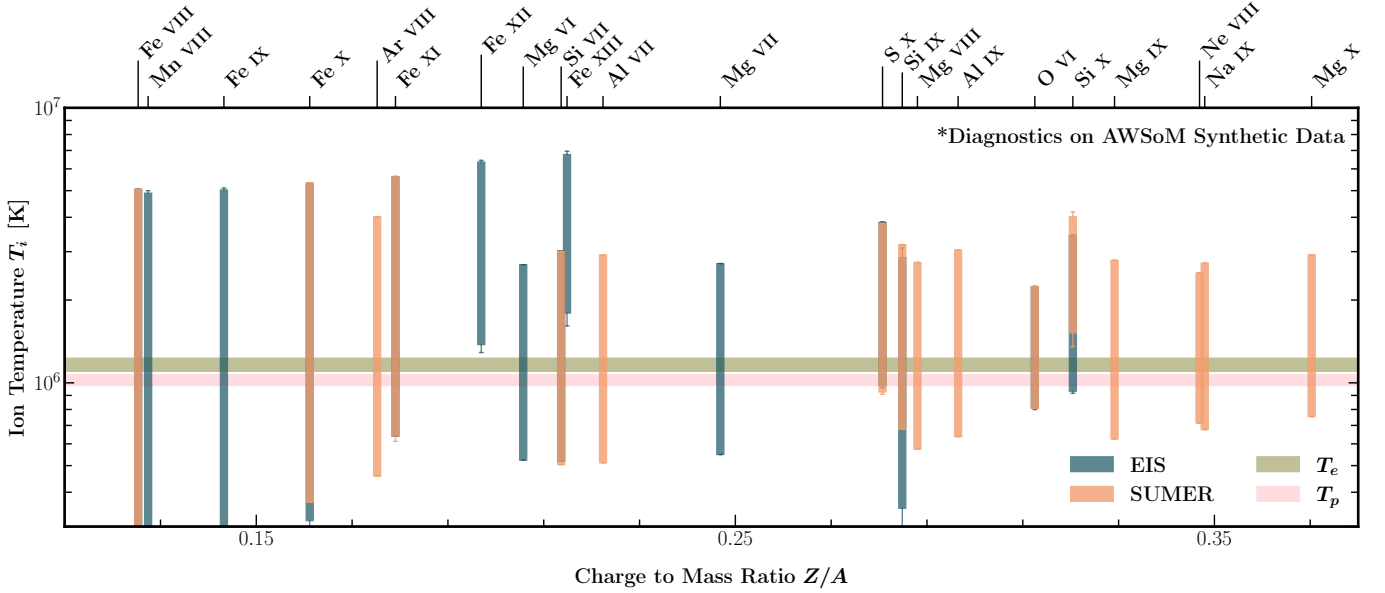
Figure 14. Ion temperature T_i diagnostics on the AWSoM-R synthetic profiles. Note that this plot is not the typical box plot to show the data distributions. The boxes show possible ion temperature intervals between $T_{i,\mathrm{min}}$ and $T_{i,\mathrm{max}}$. The whiskers indicate the uncertainty in $T_{i,\mathrm{min}}$ and $T_{i,\mathrm{max}}$. The ion temperatures inferred from lines observed by either EIS or SUMER are shown in dark green and orange, respectively. The colored horizontal area represent the range of average electron temperature T_e and proton temperature T_p along the LOS weighted by either Fe VIII 186 Å emissivity or Fe XII 192 Å emissivity. Link to the `Jupyter` notebook creating this figure ⟳.

where I_0 is the peak intensity and w_κ represents the characteristic width. w_κ is related to the FWHM of κ distribution $\Delta\lambda_\kappa$ by (see Dudík et al. 2017)

$$w_\kappa = \frac{1}{8}\frac{\Delta\lambda_\kappa^2}{(\kappa - 3/2)(2^{1/\kappa}-1)} \quad (15)$$

Figure 16 shows the SUMER line profiles fitted with a κ distribution. The κ distribution allows for an accurate fitting of the non-Gaussian wings. The reduced χ^2 with the κ distribution is much smaller than the single-Gaussian fitting but still higher than that of the double-Gaussian fitting. The three brightest doublets of O VI, Ne VIII, and Mg X show similar fitted $\kappa \sim 3-4$, except for the Ne VIII 770 Å with $\kappa \sim 8$. The fainter Mg IX 706 Å and Na IX 681 Å show larger $\kappa \sim 5$ and $\kappa \sim 8$, respectively. These κ values are slightly larger than the $\kappa \approx 1.9 - 2.5$ obtained from EIS observations to the southern polar coronal hole reported by Jeffrey et al. (2018).

As `con_width_funct_4.pro` is designed to remove the SUMER instrumental broadening from Gaussian profiles rather than κ profiles, we only gave an approximate estimate of how κ fitting would affect the measurement of $T_{i,\mathrm{max}}$ by using the line width before removing the instrumental width (see Dudík et al. 2017)

$$\frac{T_{i,\mathrm{max}}^G}{T_{i,\mathrm{max}}^\kappa} \sim \frac{(\kappa - 3/2)(2^{1/\kappa}-1)}{\ln 2}\frac{\Delta\lambda_G^2}{\Delta\lambda_\kappa^2} \quad (16)$$

where $T_{i,\mathrm{max}}^G$ is the maximum ion temperature estimated from the Gaussian FWHM $\Delta\lambda_G$, and $T_{i,\mathrm{max}}^\kappa$ is the maximum ion temperature estimated from the κ FWHM $\Delta\lambda_\kappa$. The $T_{i,\mathrm{max}}^G/T_{i,\mathrm{max}}^\kappa$ ratios of unblended O VI 1032 Å, Ne VIII 770 and 780 Å, and Mg X 609 Å are between 0.75 and 0.95, which means $T_{i,\mathrm{max}}$ might increase by 10% - 20% if the high-energy tails of the brightest SUMER lines are taken into account.

We agree with Jeffrey et al. (2018) that the non-Gaussian wings in the coronal hole might be caused by non-equilibrium ion populations, non-Gaussian turbulence, or both. We did not make further investigations into the formation mechanism of the high-energy tails, which is out of the scope of this paper.

4.4. Preferentially Heated Ions

Figure 17 compares our ion temperature T_i measurements at $\sim 1.03\,R_\odot$ at the coronal hole boundary with the two previous studies: Landi & Cranmer (2009, $1.06\,R_\odot$) and Dolla & Solomon (2008, $1.05\,R_\odot$), which both adopted UV line width observed by SUMER at the center of polar coronal holes to measure T_i. Landi & Cranmer (2009) also used the method proposed by Tu et al. (1998) to determine the possible interval of T_i. Dolla & Solomon (2008) distinguished the thermal and nonthermal widths by assuming the thermal width of Mg X 624 Å is constant at different altitudes and the

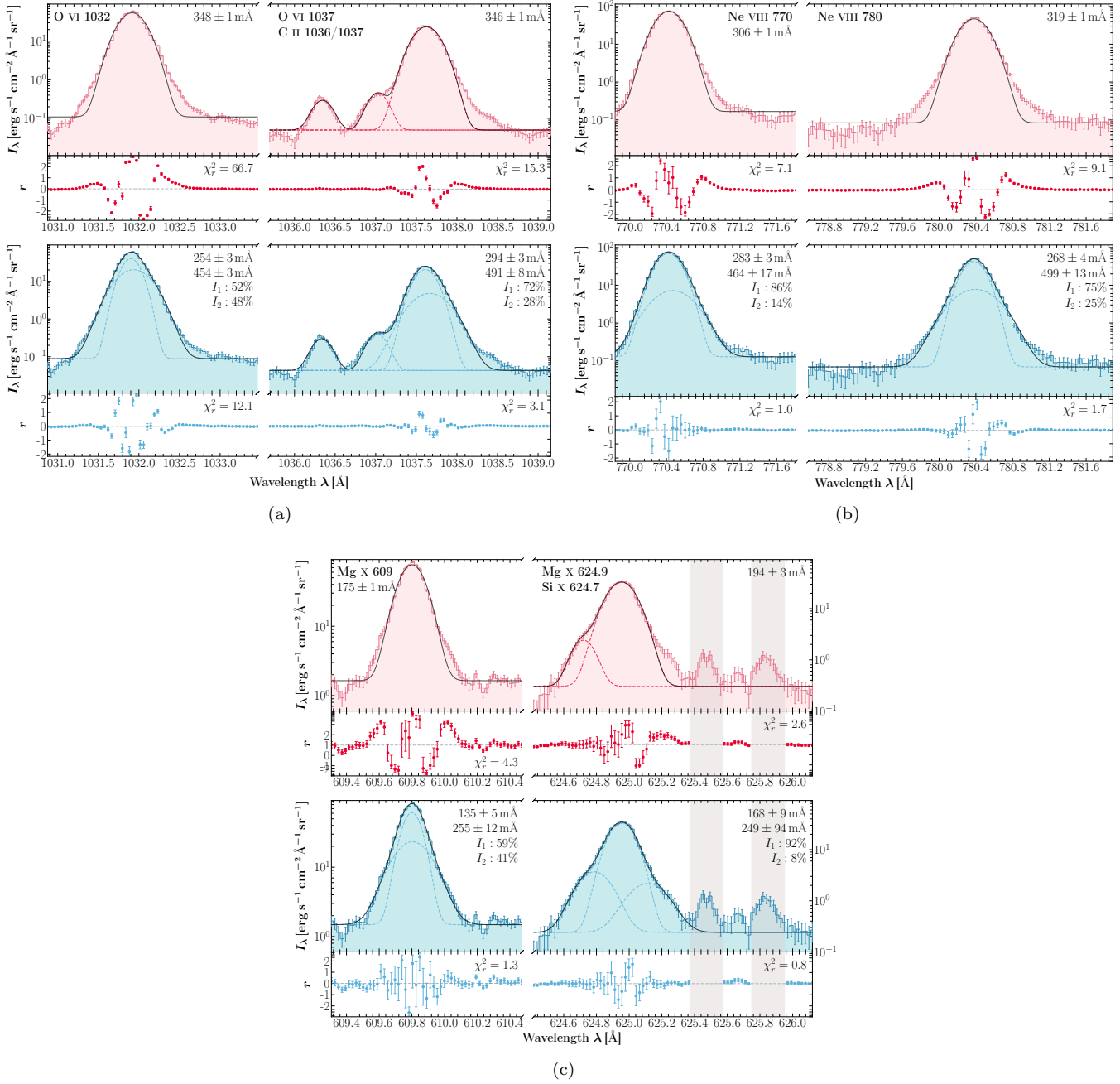**Figure 15.** Single-Gaussian and double-Gaussian fitting to the **(a)** O VI 1032 and 1037 Å, **(b)** Ne VIII 770 and 780 Å, and **(c)** Mg X 609 and 624 Å lines. The adjacent C II 1036 and 1037 Å and Si X 624 Å are also fitted. The step line shows the observed line profile. The black solid curve shows the fitting result. The dashed curves show each Gaussian component. The single-Gaussian widths, the double-Gaussian widths, and relative intensities are also shown. The vertical gray areas in panel c indicate the masked pixels during the fitting. Note that O IV 625.129 Å stray light affect the fitting of Mg X 624 Å at red wings. Link to the `Jupyter` notebook creating this figure ⦾.
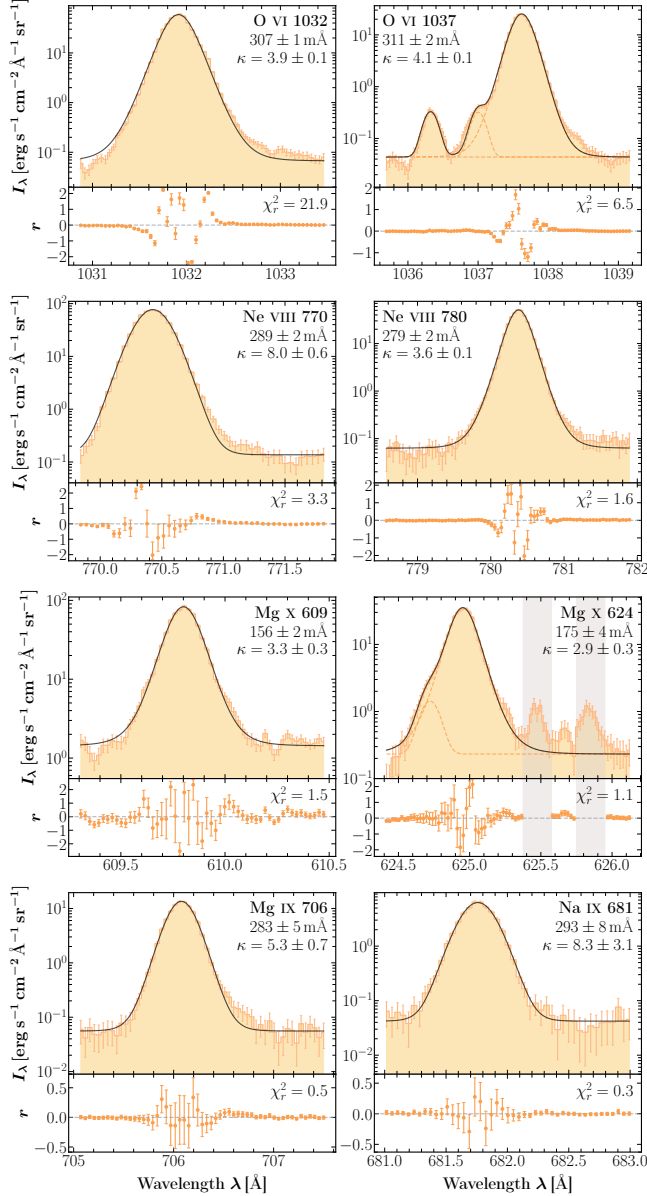
Figure 16. κ fitting of the brightest coronal lines observed by SUMER. The fitted κ and FWHM of the κ profile $\Delta\lambda_\kappa$ are shown as well. The weak blended or stray light lines are still fitted with a Gaussian distribution. Link to the `Jupyter` notebook creating this figure ⟳.

variation of nonthermal width is caused by undamped Alfvén waves.

We confirmed the U-shape dependence of T_i on Z/A in the polar coronal hole and the preferential heating of ions with $Z/A < 0.2$ or $0.33 < Z/A < 0.37$. The heating of $Z/A > 0.33$ ions is inconsistent with the traditional cascade model of ion cyclotron waves and implies additional resonant wave power at high frequencies (large Z/A, Landi & Cranmer 2009). It is worth mentioning that the high Z/A ions are only observed by SUMER,

which makes the preferential heating at $Z/A \geq 0.33$ less robust than the heating at $Z/A \leq 0.19$ recorded by both SUMER and EIS. Although most of the lower Z/A lines used in this study are observed by EIS, our results using the cross-calibrated EIS instrumental width show great consistency with the results reported by Landi & Cranmer (2009) using the same diagnostic technique. On the other hand, some of the T_i measured by Dolla & Solomon (2008) do not fall within the T_i interval found by this study, for example, Ar VIII, Fe X, Fe XII, and Na IX are found to be hotter in this study. We note that both Landi & Cranmer (2009) and this study used polar coronal hole observations during the solar minimum while the observation that Dolla & Solomon (2008) analyzed was made during the solar maximum, which might cause the differences in measured T_i, as the charge state and elemental abundances in the fast solar wind are found to vary from solar maximum to minimum (e.g., Lepri et al. 2013).

Hahn et al. (2010) analyzed the same EIS data set and applied the same ion temperature diagnostics to measure T_i from 1.04 to 1.14 $R_\odot$. They found similar preferential heating for ions with $Z/A < 0.2$. However, the heating of $Z/A > 0.33$ ions (e.g., Mg IX and Ne VIII) were not found in their study because the spectral lines of these ions can only be observed by SUMER. The EIS ion temperature intervals measured using the cross-calibrated instrumental width in this study are slightly lower than the T_i ranges reported by Hahn et al. (2010) with $\log T_{i,\max} > 7.0$. This is because Hahn et al. (2010) measured T_i at higher altitudes ($\geq 1.04\, R_\odot$) and used an old EIS instrumental width of 61 mÅ (SW detector) or 62 mÅ (LW detector).

5. CONCLUSION

The heavy ion temperatures T_i provide key information about the heating mechanism of the million-degree corona. In this study, we estimated possible T_i intervals $[T_{i,\min}, T_{i,\max}]$ at the polar coronal hole boundary simultaneously observed by Hinode/EIS and SOHO/SUMER at $\sim 1.03\, R_\odot$. We studied the dependence of T_i on the heavy ions charge-to-mass ratios (Z/A) between 0.125 and 0.37 and compared T_i with the local electron temperature T_e. We further validated our T_i diagnostic results using the line profiles synthesized from the Alfvén Wave Solar Model-realtime (AWSoM-R).

We found the heavy ions with $0.12 < Z/A < 0.2$ and $0.33 < Z/A < 0.35$ are preferentially heated at the base of the coronal hole boundary. The T_i intervals show a non-monotonic, U-shaped dependence on Z/A of heavy ions. $T_{i,\min}$ of preferentially heated ions are greater than T_e by a factor of 1.5 - 3, such as Fe VIII, Ar VIII, Mg
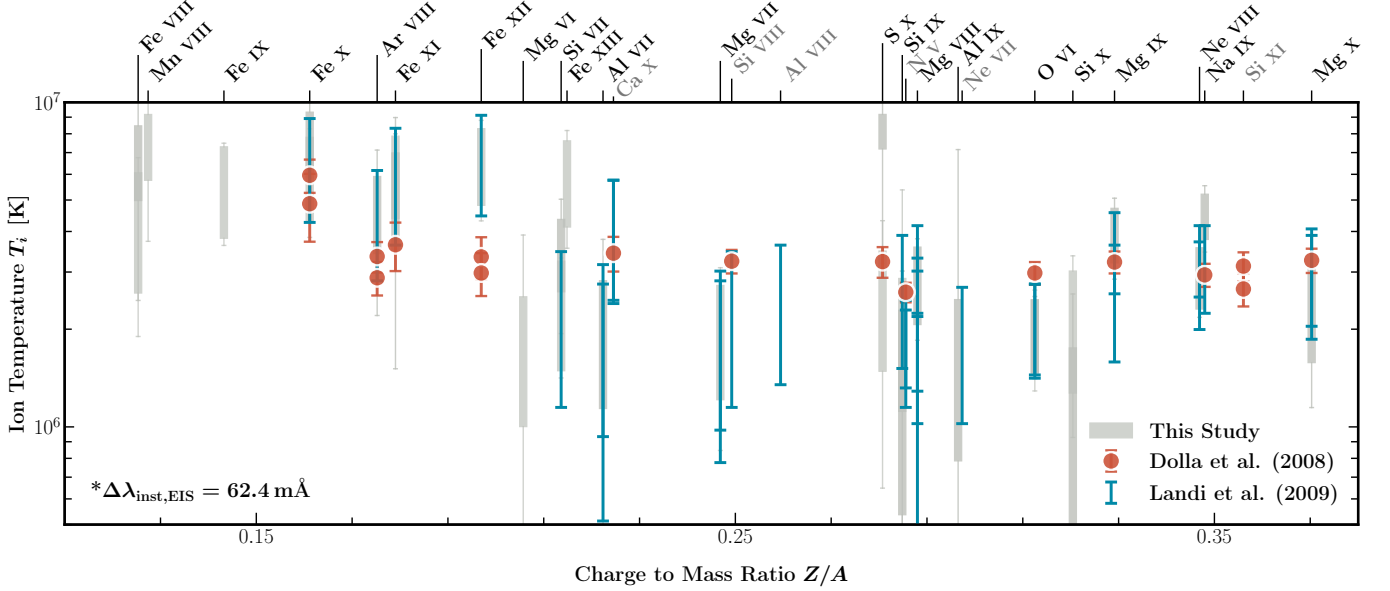
Figure 17. Comparison between the ion temperature T_i in the polar coronal hole measured by this study (grey box plot), Dolla & Solomon (2008) (red error bars), and Landi & Cranmer (2009) (blue error bars). Grey ion names represent ions that are not used in this study. Link to the `Jupyter` notebook creating this figure ⏻.

IX, and Ne VIII observed by SUMER. The T_i intervals show a non-monotonic, U-shaped dependence on Z/A of heavy ions, which is inconsistent with the traditional cascade models of the ion cyclotron resonance (Landi & Cranmer 2009).

We found the EIS instrumental width is one of the most significant contributors to the uncertainty of T_i measurement. The spectral lines observed by SUMER are $\sim 30\%$ broader than the lines from the same ion observed by EIS, when we removed the recommended EIS instrumental width $\Delta\lambda_{\mathrm{inst,EIS}} = 69.7\,\mathrm{mÅ}$. We derived a narrower EIS instrumental widths $\Delta\lambda_{\mathrm{inst,EIS}} = 62.4\,\mathrm{mÅ}$ by comparing the widths of O VI 184.1 Å and O VI 1032/1037 Å lines. The new instrumental widths provide more consistent $[T_{i,\min}, T_{i,\max}]$ measurements between EIS and SUMER.

The AWSoM-R simulation validated the preferential heating of the heavy ions and T_i diagnostic techniques. The synthetic lines of preferentially heated ions are narrower than the observed ones, probably because the ion cyclotron resonance and the heavy ion temperature are not modeled in AWSoM-R. The AWSoM-R simulation also suggests that the line profiles from hot ions, such as Fe XII and Fe XIII, might be affected by bulk velocity along the LOS.

We confirmed some of the brightest spectral lines observed by SUMER show enhanced, non-Gaussian wings in the coronal hole, including O VI, Ne VIII, and Mg X. Compared to the double-Gaussian function, κ distribution fits the lines profiles better with a $\kappa \sim 3 - 4$ for the brightest lines. If the high-energy tails are related

to the thermal velocity of heavy ions, estimated $T_{i,\max}$ might increase by another $10\% - 20\%$.

Our study reveals the complicated dependence of the ion temperature on the ion charge-to-mass ratio, which is essential to assessing coronal heating theories. We encourage future studies of the coronal ion temperatures using EUV spectral lines observed by EIS, the Spectral Imaging of the Coronal Environment (SPICE, Spice Consortium et al. 2020) instrument with the corrected point spread function (PSF), and the upcoming Solar-C (EUVST) mission (Shimizu et al. 2019), as well as the visible and infrared forbidden lines observed during the eclipse (e.g., Ding & Habbal 2017) and the NSF's Daniel K. Inouye Solar Telescope (DKIST, Rimmele et al. 2020).

APPENDIX

A. AVERAGE EFFECTIVE VELOCITY

Suppose that we have l effective velocities $v_{\mathrm{eff},1}, v_{\mathrm{eff},2}, ..., v_{\mathrm{eff},l}$ from l spectral lines of the same ion, with uncertainty $\sigma_{v,1}, \sigma_{v,2}, ..., \sigma_{v,l}$ propagated from the fitting of line widths. We assume that the uncertainty of $v_{\mathrm{eff},i}$ is independent of each other so that the measured effective velocity v_{eff} consists of two parts:

$$v_{\mathrm{eff},i} = u_{\mathrm{eff},i} + \varepsilon_i \tag{A1}$$

where $u_{\mathrm{eff},i}$ is the true effective velocity retrieved from a normal distribution with a standard deviation of σ_0 and ε_i is the random noise. We further assume that the noise ε_i follows a normal distribution with zero mean and variance of $\sigma_{v,i}^2$. Therefore, the log-likelihood function of an ion with a true effective velocity $v_{\mathrm{eff,true}}$ having l spectral lines with effective velocities of $v_{\mathrm{eff},1}, v_{\mathrm{eff},2}, ..., v_{\mathrm{eff},l}$ is

$$\ln \mathcal{L} = -\frac{1}{2} \sum_i \left[\frac{(v_{\mathrm{eff,true}} - v_{\mathrm{eff},i})^2}{\sigma_0^2 + \sigma_{v,i}^2} + \ln 2\pi(\sigma_0^2 + \sigma_{v,i}^2) \right] \tag{A2}$$

We estimate $v_{\mathrm{eff,true}}$ by the weighted average $\bar{v}_{\mathrm{eff}}$ that maximizes the likelihood function

$$\bar{v}_{\mathrm{eff}} = \sum_i w_i v_{\mathrm{eff},i} \tag{A3}$$

where

$$w_i = \frac{(\sigma_0^2 + \sigma_i^2)^{-1}}{\sum_i (\sigma_0^2 + \sigma_i^2)^{-1}} \tag{A4}$$

We then estimate the unknown σ_0 in two steps[1]: (1) We estimate σ_0, w_i, and $\bar{v}_{\mathrm{eff}}$ through an iterative method. In each iteration step $k+1$, we update the $\sigma_{0;k+1}$ by $\sigma_{0;k}$, $w_{i;k}$, and $\bar{v}_{\mathrm{eff};k}$ from the previous step k:

$$\sigma_{0;k+1}^2 = \frac{l}{l-1} \sum_i w_{i;k}(v_{\mathrm{eff},i} - \bar{v}_{\mathrm{eff};k})^2 - \sum_i \sigma_{v,i}^2 \tag{A5}$$

$\sigma_{0;k+1}$ will be set to zero if $\sigma_{0;k+1}^2 < 0$. Then we calculate the new $w_{i;k+1}$ and $\bar{v}_{\mathrm{eff};k+1}$ by

$$w_{i;k+1} = \frac{(\sigma_{0;k+1}^2 + \sigma_i^2)^{-1}}{\sum_i (\sigma_{0;k+1}^2 + \sigma_i^2)^{-1}} \tag{A6}$$

---

[1] The method is posted in a StackExchange answer https://stats.stackexchange.com/questions/454120/

and

$$\bar{v}_{\mathrm{eff};k+1} = \sum_i w_{i;k+1} v_{\mathrm{eff},i} \tag{A7}$$

The iteration stops when the relative difference between $\sigma^2_{0;k+1}$ and $\sigma^2_{0;k}$ is less than 10^{-5}.

(2) We reran a 10,000-step parametric bootstrap to give a precise estimation of the uncertainty. In each step of bootstrap, we generated $u_{\mathrm{eff},i}$ and ε_i in Eq. A1 through two normal distributions $\mathcal{N}(\mu = \bar{v}_{\mathrm{eff}}, \sigma^2 = \sigma^2_0)$ and $\mathcal{N}(\mu = 0, \sigma^2 = \sigma^2_{v,i})$, and then applied step (1) to the generated data. Finally, we update $\bar{v}_{\mathrm{eff}}$ and its uncertainty from the median and 1σ (68%) credible levels, respectively.

B. WAVELENGTH DEPENDENCE OF EIS INSTRUMENTAL WIDTHS

The latest EIS instrumental width provided by the EIS software in SolarSoft is a constant at different wavelengths. However, earlier studies of EIS instrumental width suggested that the instrumental widths in the two detectors are slightly different (e.g., Brown et al. 2008). We used the following method to investigate whether the EIS instrumental width depends on the wavelength. The fitted FHWM $\Delta\lambda_{\mathrm{fit}}$ is often interpreted as

$$\Delta\lambda^2_{\mathrm{fit}} = \Delta\lambda^2_{\mathrm{inst}} + 4\ln 2 \frac{v^2_{\mathrm{eff}}}{c^2}\lambda^2_0 \tag{B8}$$

where $\Delta\lambda_{\mathrm{inst}}$ is the instrumental FWHM. Assuming that the effective velocity $v^2_{\mathrm{eff}} = 2k_B T_i/m_i + \xi^2$ is a constant for all spectral lines of the same ion, we can treat $\Delta\lambda_{\mathrm{fit}}$ as a function of λ_0 with two parameters $\Delta\lambda_{\mathrm{inst}}$ and v_{eff}, i.e., $\Delta\lambda_{\mathrm{fit}} = f(\lambda_0 | \Delta\lambda_{\mathrm{inst}}, v_{\mathrm{eff}})$. If $\Delta\lambda_{\mathrm{inst}}$ does not depend on the wavelength, we could use $(\Delta\lambda_{\mathrm{fit}}, \lambda_0)$ pairs from different spectral lines of the same ion to fit $\Delta\lambda_{\mathrm{inst}}$ and v_{eff}.

We implemented this method on an EIS data set observing the west off-limb quiet Sun corona on 2007 April 13. The data set has been studied in Landi & Young (2010) to cross-calibrate the intensity between EIS and SUMER. We averaged the data of the same 30 pixels on the CCD detector used in the coronal hole study. Although there are not many isolated and strong lines of the same ion observed by EIS, we found that the Fe XI and Fe XII lines are the best candidates to implement this method. Figure B1 shows the fitted FWHM $\Delta\lambda_{\mathrm{fit}}$ and line centroid wavelength λ_0 of the Fe XI and Fe XII lines. For Fe XI lines, we obtained a instrumental widths $\Delta\lambda_{\mathrm{inst}} = 71.9 \pm 1.2\,\mathrm{m\AA}$, which is more consistent with the instrumental widths $\Delta\lambda_{\mathrm{inst}} = 69.7\,\mathrm{m\AA}$ given by the EIS software. However, there are some outliers in the Fe XI lines, including the Fe XI 181.130 Å and 257.772 Å. The Fe XII triplets at 192.394, 193.509 and 195.119, Å have very similar line widths $\Delta\lambda_{\mathrm{fit}} \sim 77\,\mathrm{m\AA}$. However, the line widths $\Delta\lambda_{\mathrm{fit}}$ of Fe XII 249.388, 259.973, and 291.010 Å line does show a monotonic dependence on λ_0. Therefore, we cannot fit Fe XII line widths versus wavelength to obtain the instrumental width. We suggest that the instrumental width of the EIS 2″ slit might depend on the wavelength.
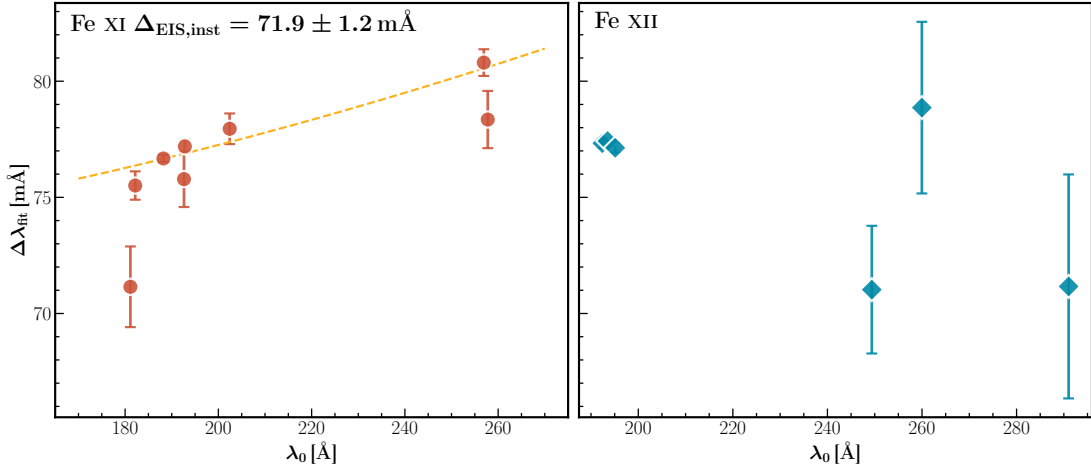

Figure B1. Fitted FWHM $\Delta\lambda_{\mathrm{fit}}$ versus line centroid wavelength λ_0 of the Fe XI and Fe XII lines in off-limb quiet Sun corona. The dashed line in the left panel shows the best fitting of $\Delta\lambda_{\mathrm{fit}} = f(\lambda_0 | \Delta\lambda_{\mathrm{inst}}, v_{\mathrm{eff}})$. Link to the `Jupyter` notebook creating this figure ⟲.

C. TABLE OF LINE WIDTHS

Table C1. Estimated ranges of ion temperatures $T_{i,\min}$ and $T_{i,\max}$, average effective velocity $\bar{v}_{\rm eff}$, the fitted line width $\Delta\lambda_{\rm fit}$, and the width after the removal of instrumental width $\Delta\lambda_{\rm true}$. Quantities with * are calculated using the EIS instrumental width $\Delta\lambda'_{\rm inst,EIS} = 62.4$ mÅ cross-calibrated from SUMER observations. The fitting of the individual spectral line can be found in the following Jupyter notebooks: EIS, SUMER window 1, SUMER window 2, SUMER window 3, and SUMER window 4.

Ion	Z/A	Inst.	Instrument Averaged Values						Individual Line Measurements			
			$\log T_{i,\min}$ [K]	$\log T_{i,\max}$ [K]	$\log T^*_{i,\min}$ [K]	$\log T^*_{i,\max}$ [K]	$\bar{v}_{\rm eff}$ [km s^{-1}]	$\bar{v}^*_{\rm eff}$ [km s^{-1}]	λ [Å]	$\Delta\lambda_{\rm true}$ [mÅ]	$\Delta\lambda^*_{\rm true}$ [mÅ]	$\Delta\lambda_{\rm fit}$ [mÅ]
Fe VIII	0.125	EIS	....	$6.54^{+0.05}_{-0.05}$	$6.41^{+0.10}_{-0.13}$	$6.78^{+0.05}_{-0.05}$	$32.2^{+1.8}_{-1.9}$	42.5 ± 2.4	185.213	31.4 ± 1.1	44.1 ± 0.8	76.48 ± 0.45
									186.598	38.8 ± 1.5	49.7 ± 1.1	79.79 ± 0.71
									194.661	33.1 ± 1.1	45.3 ± 0.8	77.16 ± 0.49
									253.956	39.6 ± 5.6	49.7 ± 4.5	79.8 ± 2.8
		SUMER	$6.70^{+0.18}_{-0.31}$	$6.93^{+0.11}_{-0.15}$	....	....	50.2 ± 7.5	....	697.156	194 ± 29	....	281 ± 20
Mn VIII	0.127	EIS	$6.45^{+0.23}_{-0.55}$	$6.79^{+0.12}_{-0.17}$	$6.76^{+0.13}_{-0.19}$	$6.96^{+0.09}_{-0.11}$	43.4 ± 7.0	52.8 ± 5.8	185.455	44.7 ± 7.2	54.4 ± 5.9	82.8 ± 3.9
Fe IX	0.143	EIS	$6.07^{+0.06}_{-0.07}$	$6.67^{+0.02}_{-0.02}$	$6.58^{+0.02}_{-0.02}$	$6.86^{+0.01}_{-0.01}$	37.2 ± 0.7	46.6 ± 0.6	191.206	33.1 ± 4.2	45.2 ± 3.1	77.1 ± 1.8
									197.854	41.0 ± 0.7	51.3 ± 0.6	80.85 ± 0.35
Fe X	0.161	EIS	$6.09^{+0.11}_{-0.15}$	$6.67^{+0.03}_{-0.03}$	$6.64^{+0.05}_{-0.05}$	$6.89^{+0.03}_{-0.03}$	37.5 ± 1.4	48.2 ± 1.5	174.531	38.0 ± 3.1	49.0 ± 2.4	79.4 ± 1.5
									177.240	40.7 ± 1.3	51.2 ± 1.0	80.8 ± 0.6
									184.537	37.1 ± 0.6	48.4 ± 0.4	79.0 ± 0.3
									190.037	38.0 ± 1.0	50.4 ± 0.8	80.3 ± 0.5
									193.715	34.6 ± 2.7	46.4 ± 2.0	77.8 ± 1.2
		SUMER	$6.77^{+0.06}_{-0.07}$	$6.97^{+0.04}_{-0.04}$	....	....	52.7 ± 2.3	....	1028.053	301 ± 13	....	355 ± 11
									1028.082			
Ar VIII	0.175	SUMER	$6.53^{+0.13}_{-0.19}$	$6.77^{+0.08}_{-0.10}$	....	....	49.6 ± 5.1	....	713.801	197 ± 20	....	282 ± 14
Fe XI	0.179	EIS	$6.16^{+0.04}_{-0.04}$	$6.69^{+0.01}_{-0.01}$	$6.64^{+0.01}_{-0.01}$	$6.90^{+0.01}_{-0.01}$	38.3 ± 0.5	48.4 ± 0.4	182.167	39.6 ± 3.0	50.3 ± 2.4	80.2 ± 1.5
									188.216	39.9 ± 0.7	50.5 ± 0.5	80 ± 0.3
									188.299	39.9 ± 0.7	50.5 ± 0.5	80 ± 0.3
									192.627	42.7 ± 3.1	52.7 ± 2.5	81.7 ± 1.6
									202.424	51.4 ± 5.1	60.0 ± 4.3	86.6 ± 3.0
		SUMER	$6.54^{+0.20}_{-0.37}$	$6.84^{+0.11}_{-0.15}$	....	....	45.6 ± 6.5	....	1028.955	260 ± 37	....	322 ± 30
Fe XII	0.197	EIS	$6.31^{+0.10}_{-0.13}$	$6.74^{+0.04}_{-0.04}$	$6.68^{+0.04}_{-0.05}$	$6.92^{+0.03}_{-0.03}$	$40.6^{+1.8}_{-1.9}$	49.7 ± 1.5	192.394	41.9 ± 4.7	52.1 ± 3.7	81.3 ± 2.4
									193.509	40.4 ± 1.0	50.9 ± 0.8	80.6 ± 0.5
									195.119	47.5 ± 0.9	56.7 ± 0.8	84.4 ± 0.5
Mg VI	0.206	EIS	$5.61^{+0.64}_{-}$	$6.28^{+0.23}_{-0.55}$	$6.00^{+0.38}_{-}$	$6.40^{+0.19}_{-0.35}$	36.3 ± 13.0	41.5 ± 11.4	268.991	54 ± 19	62.0 ± 17.0	88 ± 12

Table C1 *continued*

Table C1 (*continued*)

Ion	Z/A	Inst.	Instrument Averaged Values						Individual Line Measurements			
			$\log T_{i,\min}$ [K]	$\log T_{i,\max}$ [K]	$\log T^*_{i,\min}$ [K]	$\log T^*_{i,\max}$ [K]	$\bar{v}_{\rm eff}$ [km s^{-1}]	$\bar{v}^*_{\rm eff}$ [km s^{-1}]	λ [Å]	$\Delta\lambda_{\rm true}$ [mÅ]	$\Delta\lambda^*_{\rm true}$ [mÅ]	$\Delta\lambda_{\rm fit}$ [mÅ]
Si VII	0.214	EIS	$5.93^{+0.03}_{-0.04}$	$6.41^{+0.01}_{-0.01}$	$6.42^{+0.10}_{-0.13}$	$6.64^{+0.06}_{-0.07}$	39.2 ± 0.5	43.8 ± 0.5	272.647	59.4 ± 2.3	66.5 ± 2.1	91.2 ± 1.5
									275.361	60.1 ± 0.8	67.1 ± 0.7	91.7 ± 0.5
									275.675	56.9 ± 4.1	64.3 ± 3.6	89.6 ± 2.6
		SUMER	$6.42^{+0.10}_{-0.13}$	$6.64^{+0.06}_{-0.07}$	...	...	50.8 ± 3.9	...	1049.153	296 ± 23	...	352 ± 19
Fe XIII	0.215	EIS	$6.20^{+0.13}_{-0.20}$	$6.70^{+0.05}_{-0.05}$	$6.62^{+0.06}_{-0.07}$	$6.88^{+0.03}_{-0.03}$	38.8 ± 2.2	47.6 ± 1.8	202.044	43.5 ± 2.5	53.4 ± 2.0	82.2 ± 1.3
Al VII	0.222	SUMER	$6.06^{+0.27}_{-0.81}$	$6.45^{+0.13}_{-0.18}$	...	...	41.7 ± 7.1	...	1053.996	244 ± 42	...	307 ± 33
Mg VII	0.247	EIS	$5.83^{+0.19}_{-0.33}$	$6.34^{+0.07}_{-0.08}$	$6.08^{+0.11}_{-0.16}$	$6.44^{+0.05}_{-0.06}$	38.7 ± 3.2	43.2 ± 2.9	276.154	59.3 ± 4.9	66.3 ± 4.4	91.1 ± 3.2
S X	0.281	EIS	$5.83^{+0.36}$	$6.43^{+0.12}_{-0.17}$	$6.17^{+0.19}_{-0.36}$	$6.54^{+0.09}_{-0.12}$	$37.2^{+5.9}_{-5.6}$	$42.5^{+5.1}_{-5.0}$	259.496	61 ± 15	67.6 ± 14	92 ± 10
									264.230	52.0 ± 9.7	60.0 ± 8.4	86.6 ± 5.8
		SUMER	$6.86^{+0.19}_{-0.35}$	$6.96^{+0.16}_{-0.25}$	...	...	69.4 ± 15.0	...	776.373	299 ± 65	...	358 ± 54
Si IX	0.285	EIS	$5.52^{+0.93}$	$6.32^{+0.34}$	$6.05^{+0.51}$	$6.46^{+0.27}_{-0.90}$	35.1 ± 21.5	41.2 ± 18.3	258.080	50 ± 31	59.1 ± 26.2	86 ± 18
		SUMER	$5.73^{+0.37}$	$6.36^{+0.12}_{-0.17}$	...	...	36.8 ± 5.9	...	694.686	142 ± 23	...	249 ± 13
Mg VIII	0.288	SUMER	$6.32^{+0.04}_{-0.05}$	$6.55^{+0.03}_{-0.03}$	...	...	49.5 ± 1.5	...	689.641	187 ± 27	...	276 ± 18
									762.660	163 ± 38	...	258 ± 24
									772.260	197 ± 12	...	280.2 ± 8.6
									782.362	222.9 ± 7.8	...	298.4 ± 5.8
Al IX	0.296	SUMER	$5.90^{+0.84}$	$6.39^{+0.46}$	...	...	39.4 ± 36.6	...	703.73	154 ± 143	...	256 ± 86
		EIS	$5.77^{+0.12}_{-0.16}$	$6.20^{+0.05}_{-0.05}$	$6.17^{+0.05}_{-0.06}$	$6.39^{+0.03}_{-0.03}$	40.6 ± 2.3	50.6 ± 1.8	184.117	41.5 ± 2.3	51.7 ± 1.9	81.1 ± 1.2
O VI	0.313	SUMER	$6.17^{+0.02}_{-0.02}$	$6.39^{+0.01}_{-0.01}$	...	...	50.6 ± 0.6	...	1031.912	294.4 ± 3.3	...	350.2 ± 2.8
									1037.613	288.8 ± 1.2	...	345.6 ± 1.0
Si X	0.320	EIS	$5.75^{+0.21}_{-0.42}$	$6.36^{+0.06}_{-0.07}$	$6.10^{+0.10}_{-0.14}$	$6.48^{+0.05}_{-0.05}$	$37.0^{+2.7}_{-2.8}$	$42.3^{+2.4}_{-2.3}$	258.374	54.0 ± 4.2	61.7 ± 3.7	87.8 ± 2.6
									261.056	49.5 ± 8.1	57.8 ± 6.9	85.1 ± 4.7
		SUMER	...	$6.24^{+0.17}_{-0.27}$	...	...	32.2 ± 7.5	...	624.694	112 ± 26	...	145 ± 20
Mg IX	0.329	SUMER	$6.51^{+0.04}_{-0.05}$	$6.67^{+0.03}_{-0.03}$	...	...	56.8 ± 2.1	...	706.060	228.5 ± 4.7	...	305.0 ± 3.5
									749.552	223 ± 13	...	300.9 ± 9.2
Ne VIII	0.347	SUMER	$6.36^{+0.02}_{-0.03}$	$6.55^{+0.02}_{-0.02}$	...	...	54.2 ± 1.0	...	770.428	228.2 ± 2.3	...	302.3 ± 1.7
									780.385	239.8 ± 3.9	...	311.0 ± 3.0
Na IX	0.348	SUMER	$6.58^{+0.04}_{-0.04}$	$6.72^{+0.03}_{-0.03}$	...	...	61.4 ± 1.9	...	681.719	232.5 ± 7.2	...	308.0 ± 5.4
Mg X	0.370	SUMER	$6.20^{+0.10}_{-0.14}$	$6.49^{+0.06}_{-0.07}$	...	...	$46.0^{+3.1}_{-3.2}$	...	609.793	145.1 ± 2.6	...	171.4 ± 2.2
									624.941	170.6 ± 3.4	...	193.3 ± 3.0

REFERENCES

Akinari, N. 2007, ApJ, 660, 1660, doi: 10.1086/512844

Astropy Collaboration, Robitaille, T. P., Tollerud, E. J.,
et al. 2013, A&A, 558, A33,
doi: 10.1051/0004-6361/201322068

Astropy Collaboration, Price-Whelan, A. M., Sipőcz, B. M.,
et al. 2018, AJ, 156, 123, doi: 10.3847/1538-3881/aabc4f

Boland, B. C., Dyer, E. P., Firth, J. G., et al. 1975,
MNRAS, 171, 697, doi: 10.1093/mnras/171.3.697

Bowen, T. A., Mallet, A., Huang, J., et al. 2020, ApJS, 246,
66, doi: 10.3847/1538-4365/ab6c65

Brown, C. M., Feldman, U., Seely, J. F., Korendyke, C. M.,
& Hara, H. 2008, ApJS, 176, 511, doi: 10.1086/529378

Chae, J., Schühle, U., & Lemaire, P. 1998, ApJ, 505, 957,
doi: 10.1086/306179

Crameri, F. 2021, Scientific colour maps, 7.0.1, Zenodo,
Zenodo, doi: 10.5281/zenodo.1243862

Cranmer, S. R. 2009, Living Reviews in Solar Physics, 6, 3,
doi: 10.12942/lrsp-2009-3

Cranmer, S. R., Field, G. B., & Kohl, J. L. 1999, ApJ, 518,
937, doi: 10.1086/307330

Cranmer, S. R., van Ballegooijen, A. A., & Edgar, R. J.
2007, ApJS, 171, 520, doi: 10.1086/518001

Culhane, J. L., Harra, L. K., James, A. M., et al. 2007,
SoPh, 243, 19, doi: 10.1007/s01007-007-0293-1

Del Zanna, G. 2013, A&A, 555, A47,
doi: 10.1051/0004-6361/201220810

Del Zanna, G., Dere, K. P., Young, P. R., & Landi, E. 2021,
ApJ, 909, 38, doi: 10.3847/1538-4357/abd8ce

Del Zanna, G., Gupta, G. R., & Mason, H. E. 2019, A&A,
631, A163, doi: 10.1051/0004-6361/201834625

Del Zanna, G., & Mason, H. E. 2018, Living Reviews in
Solar Physics, 15, 5, doi: 10.1007/s41116-018-0015-3

Delaboudinière, J. P., Artzner, G. E., Brunaud, J., et al.
1995, SoPh, 162, 291, doi: 10.1007/BF00733432

Dere, K. P., Landi, E., Mason, H. E., Monsignori Fossi,
B. C., & Young, P. R. 1997, A&AS, 125, 149,
doi: 10.1051/aas:1997368

Ding, A., & Habbal, S. R. 2017, ApJL, 842, L7,
doi: 10.3847/2041-8213/aa7460

Dolla, L., & Solomon, J. 2008, A&A, 483, 271,
doi: 10.1051/0004-6361:20077903

—. 2009, Annales Geophysicae, 27, 3551,
doi: 10.5194/angeo-27-3551-2009

Domingo, V., Fleck, B., & Poland, A. I. 1995, SoPh, 162, 1,
doi: 10.1007/BF00733425

Doyle, J. G., Teriaca, L., & Banerjee, D. 1999, A&A, 349,
956

Dudík, J., & Dzifčáková, E. 2021, in Astrophysics and
Space Science Library, Vol. 464, Kappa Distributions;
From Observational Evidences via Controversial
Predictions to a Consistent Theory of Nonequilibrium
Plasmas, ed. M. Lazar & H. Fichtner, 53–87,
doi: 10.1007/978-3-030-82623-9_4

Dudík, J., Polito, V., Dzifčáková, E., Del Zanna, G., &
Testa, P. 2017, ApJ, 842, 19,
doi: 10.3847/1538-4357/aa71a8

Esser, R., Fineschi, S., Dobrzycka, D., et al. 1999, ApJL,
510, L63, doi: 10.1086/311786

Esser, R., Holzer, T. E., & Leer, E. 1987, J. Geophys. Res.,
92, 13377, doi: 10.1029/JA092iA12p13377

Foreman-Mackey, D. 2016, The Journal of Open Source
Software, 1, 24, doi: 10.21105/joss.00024

Freeland, S. L., & Handy, B. N. 2012, SolarSoft:
Programming and data analysis environment for solar
physics. http://ascl.net/1208.013

Gilly, C. R., & Cranmer, S. R. 2020, ApJ, 901, 150,
doi: 10.3847/1538-4357/abb1ad

Hahn, M., Bryans, P., Landi, E., Miralles, M. P., & Savin,
D. W. 2010, ApJ, 725, 774,
doi: 10.1088/0004-637X/725/1/774

Hahn, M., Landi, E., & Savin, D. W. 2012, ApJ, 753, 36,
doi: 10.1088/0004-637X/753/1/36

Hahn, M., & Savin, D. W. 2013a, ApJ, 763, 106,
doi: 10.1088/0004-637X/763/2/106

—. 2013b, ApJ, 776, 78, doi: 10.1088/0004-637X/776/2/78

—. 2014, ApJ, 795, 111, doi: 10.1088/0004-637X/795/2/111

Harvey, J. W., Hill, F., Hubbard, R. P., et al. 1996,
Science, 272, 1284, doi: 10.1126/science.272.5266.1284

Hassler, D. M., Rottman, G. J., Shoub, E. C., & Holzer,
T. E. 1990, ApJL, 348, L77, doi: 10.1086/185635

Hassler, D. M., Wilhelm, K., Lemaire, P., & Schühle, U.
1997, SoPh, 175, 375, doi: 10.1023/A:1004959324214

Hollweg, J. V., & Isenberg, P. A. 2002, Journal of
Geophysical Research (Space Physics), 107, 1147,
doi: 10.1029/2001JA000270

Hu, Y. Q., Esser, R., & Habbal, S. R. 2000,
J. Geophys. Res., 105, 5093, doi: 10.1029/1999JA900430

Hu, Y. Q., & Habbal, S. R. 1999, J. Geophys. Res., 104,
17045, doi: 10.1029/1999JA900193

Hunter, J. D. 2007, Computing in Science & Engineering, 9,
90, doi: 10.1109/MCSE.2007.55

Isenberg, P. A., & Hollweg, J. V. 1983, J. Geophys. Res.,
88, 3923, doi: 10.1029/JA088iA05p03923

Isenberg, P. A., & Vasquez, B. J. 2007, ApJ, 668, 546,
doi: 10.1086/521220

—. 2009, ApJ, 696, 591, doi: 10.1088/0004-637X/696/1/591

Jeffrey, N. L. S., Hahn, M., Savin, D. W., & Fletcher, L. 2018, ApJL, 855, L13, doi: 10.3847/2041-8213/aab08c

Kasper, J. C., Maruca, B. A., Stevens, M. L., & Zaslavsky, A. 2013, PhRvL, 110, 091102, doi: 10.1103/PhysRevLett.110.091102

Kohl, J. L., Esser, R., Gardner, L. D., et al. 1995, SoPh, 162, 313, doi: 10.1007/BF00733433

Kohl, J. L., Noci, G., Antonucci, E., et al. 1997, SoPh, 175, 613, doi: 10.1023/A:1004903206467

—. 1998, ApJL, 501, L127, doi: 10.1086/311434

Kosugi, T., Matsuzaki, K., Sakao, T., et al. 2007, SoPh, 243, 3, doi: 10.1007/s11207-007-9014-6

Landi, E. 2007, ApJ, 663, 1363, doi: 10.1086/517910

Landi, E., & Cranmer, S. R. 2009, ApJ, 691, 794, doi: 10.1088/0004-637X/691/1/794

Landi, E., & Young, P. R. 2010, ApJ, 714, 636, doi: 10.1088/0004-637X/714/1/636

Lazar, M., Fichtner, H., & Yoon, P. H. 2016, A&A, 589, A39, doi: 10.1051/0004-6361/201527593

Lepri, S. T., Landi, E., & Zurbuchen, T. H. 2013, ApJ, 768, 94, doi: 10.1088/0004-637X/768/1/94

Li, X., Habbal, S. R., Kohl, J. L., & Noci, G. 1998, ApJL, 501, L133, doi: 10.1086/311428

Lionello, R., Linker, J. A., & Mikić, Z. 2001, ApJ, 546, 542, doi: 10.1086/318254

Markovskii, S. A., & Hollweg, J. V. 2004, ApJ, 609, 1112, doi: 10.1086/421323

Marsch, E., Goertz, C. K., & Richter, K. 1982, J. Geophys. Res., 87, 5030, doi: 10.1029/JA087iA07p05030

Olbert, S. 1968, in Astrophysics and Space Science Library, Vol. 10, Physics of the Magnetosphere, ed. R. D. L. Carovillano & J. F. McClay, 641, doi: 10.1007/978-94-010-3467-8_23

Oliphant, T. E. 2006, A guide to NumPy, Vol. 1 (Trelgol Publishing USA)

Patsourakos, S., Habbal, S. R., & Hu, Y. Q. 2002, ApJL, 581, L125, doi: 10.1086/345976

Pauluhn, A., Rüedi, I., Solanki, S. K., et al. 2001, ApOpt, 40, 6292, doi: 10.1364/AO.40.006292

Peter, H., & Judge, P. G. 1999, ApJ, 522, 1148, doi: 10.1086/307672

Rimmele, T. R., Warner, M., Keil, S. L., et al. 2020, SoPh, 295, 172, doi: 10.1007/s11207-020-01736-7

Seely, J. F., Feldman, U., Schühle, U., et al. 1997, ApJL, 484, L87, doi: 10.1086/310769

Shimizu, T., Imada, S., Kawate, T., et al. 2019, in Society of Photo-Optical Instrumentation Engineers (SPIE) Conference Series, Vol. 11118, UV, X-Ray, and Gamma-Ray Space Instrumentation for Astronomy XXI, 1111807, doi: 10.1117/12.2528240

Sokolov, I. V., Holst, B. v. d., Manchester, W. B., et al. 2021, ApJ, 908, 172, doi: 10.3847/1538-4357/abc000

Spice Consortium, Anderson, M., Appourchaux, T., et al. 2020, A&A, 642, A14, doi: 10.1051/0004-6361/201935574

Szente, J., Landi, E., Manchester, W. B., I., et al. 2019, ApJS, 242, 1, doi: 10.3847/1538-4365/ab16d0

The SunPy Community, Barnes, W. T., Bobra, M. G., et al. 2020, The Astrophysical Journal, 890, 68, doi: 10.3847/1538-4357/ab4f7a

Tóth, G., van der Holst, B., Sokolov, I. V., et al. 2012, Journal of Computational Physics, 231, 870, doi: 10.1016/j.jcp.2011.02.006

Tu, C. Y., & Marsch, E. 1997, SoPh, 171, 363, doi: 10.1023/A:1004968327196

Tu, C. Y., Marsch, E., & Wilhelm, K. 1999, SSRv, 87, 331, doi: 10.1023/A:1005154030100

Tu, C. Y., Marsch, E., Wilhelm, K., & Curdt, W. 1998, ApJ, 503, 475, doi: 10.1086/305982

van der Holst, B., Sokolov, I. V., Meng, X., et al. 2014, ApJ, 782, 81, doi: 10.1088/0004-637X/782/2/81

Van Der Walt, S., Colbert, S. C., & Varoquaux, G. 2011, Computing in Science & Engineering, 13, 22

Vasyliunas, V. M. 1968, J. Geophys. Res., 73, 2839, doi: 10.1029/JA073i009p02839

Vernazza, J. E., & Reeves, E. M. 1978, ApJS, 37, 485, doi: 10.1086/190539

Virtanen, P., Gommers, R., Oliphant, T. E., et al. 2020, Nature Methods, 17, 261, doi: https://doi.org/10.1038/s41592-019-0686-2

Warren, H. P., Ugarte-Urra, I., & Landi, E. 2014, ApJS, 213, 11, doi: 10.1088/0067-0049/213/1/11

Wilhelm, K. 1999, Ap&SS, 264, 43, doi: 10.1023/A:1002411723017

—. 2012, SSRv, 172, 57, doi: 10.1007/s11214-010-9700-9

Wilhelm, K., Fludra, A., Teriaca, L., et al. 2005, A&A, 435, 733, doi: 10.1051/0004-6361:20042460

Wilhelm, K., Marsch, E., Dwivedi, B. N., et al. 1998, ApJ, 500, 1023, doi: 10.1086/305756

Wilhelm, K., Curdt, W., Marsch, E., et al. 1995, SoPh, 162, 189, doi: 10.1007/BF00733430

Withbroe, G. L., & Noyes, R. W. 1977, ARA&A, 15, 363, doi: 10.1146/annurev.aa.15.090177.002051

Young, P. 2010, EIS Software Note No. 4 - Slit tilts. http://solarb.mssl.ucl.ac.uk/SolarB/eis_docs/eis_notes/04_SLIT_TILT/eis_swnote_04.pdf

—. 2011a, EIS Software Note No. 3 - Spatial Y-offsets

between different wavelengths (spectrum tilt and CCD

offset).

http://solarb.mssl.ucl.ac.uk/SolarB/eis_docs/eis_notes/

03_GRATING_DETECTOR_TILT/eis_swnote_03.pdf

—. 2011b, EIS Software Note No. 7 - Instrumental line
widths for the narrow slits of EIS.
http://solarb.mssl.ucl.ac.uk/SolarB/eis_docs/eis_notes/
07_LINE_WIDTH/eis_swnote_07.pdf

—. 2019, EIS Software Note No. 1 - Calibrating EIS data:
the EIS_PREP routine.
http://solarb.mssl.ucl.ac.uk/SolarB/eis_docs/eis_notes/
01_EIS_PREP/eis_swnote_01.pdf

Young, P. R., Watanabe, T., Hara, H., & Mariska, J. T.
2009, A&A, 495, 587, doi: 10.1051/0004-6361:200810143